HHS Public Access

Author manuscript

Circ Res. Author manuscript; available in PMC 2025 May 10.

Published in final edited form as:

Circ Res. 2024 May 10; 134(10): 1330–1347. doi:10.1161/CIRCRESAHA.123.323190.

CD151 Maintains Endolysosomal Protein Quality to Inhibit Vascular Inflammation

Junxiong Chen[1], **Yingjun Ding**[1,#], **Chao Jiang**[1,#], **Rongmei Qu**[1], **Jonathan D. Wren**[2], **Constantin Georgescu**[2], **Xuejun Wang**[1], **Darlene N. Reuter**[1], **Beibei Liu**[1], **Cory B. Giles**[2], **Christoph H. Mayr**[3], **Herbert B. Schiller**[3], **Jingxing Dai**[1], **Christopher S. Stipp**[4], **Bharathiraja Subramaniyan**[1], **Jie Wang**[1], **Houjuan Zuo**[1], **Chao Huang**[1], **Kar-Ming Fung**[1], **Heather C. Rice**[1], **Arnoud Sonnenberg**[5], **David Wu**[6], **Matthew S. Walters**[1], **You-Yang Zhao**[7,8], **Tomoharu Kanie**[1], **Franklin A. Hays**[1], **James F. Papin**[1], **Dao Wen Wang**[9,*], **Xin A. Zhang**[1,10,*]

[1]University of Oklahoma Health Sciences Center, Oklahoma City, USA

[2]Oklahoma Medical Research Foundation, Oklahoma City, USA

[3]Helmholtz Munich, Munich, Germany

[4]University of Iowa, Iowa City, Iowa, USA

[5]Netherlands Cancer Institute, Amsterdam, Netherlands

[6]University of Chicago, Chicago, IL, USA

[7]Ann & Robert H. Lurie Children's Hospital of Chicago, Chicago, Illinois

[8]Northwestern University Feinberg School of Medicine, Chicago, Illinois

[9]Tongji Hospital, Huazhong University of Science and Technology, Wuhan, China

[10]Lead contact

Abstract

Background: Tetraspanin CD151 is highly expressed in endothelia and reinforces cell adhesion, but its role in vascular inflammation remains largely unknown.

Methods: *In vitro* molecular and cellular biological analyses on genetically modified endothelial cells, *in vivo* vascular biological analyses on genetically engineered mouse models, and *in silico* systems biology and bioinformatics analyses on CD151-related events.

Results: Endothelial ablation of *Cd151* leads to pulmonary and cardiac inflammation, severe sepsis, and perilous Covid19 and that endothelial CD151 becomes downregulated in inflammation.

*Correspondence: xin-zhang-1@ouhsc.edu and dwwang@tjh.tjmu.edu.cn.
#These authors made equal contributions to this study.

Author Contributions

J.C. designed and performed experiments, analyzed data, and wrote the manuscript. Y.D., C.J., R.Q., and J.D. performed experiments. J.D.W., C.G., and C.B.G. performed bioinformatics analysis. X.W., J.W., and H.Z. maintained mice models. C.H.M. and H.B.S. performed lung tissue proteomics. C.S.S., A.S., D. W. and Y.Y.Z. provided special reagents. Y.Y.Z. and K.F. provided technical advice. D.W. designed some experiments. X.A.Z conceived and supervised the study, designed the experiments, and wrote the manuscript.

Disclosures

None.

Mechanistically, CD151 restrains endothelial release of pro-inflammatory molecules for less leukocyte infiltration. At the subcellular level, CD151 determines the integrity of multi-vesicular bodies (MVBs)/lysosomes and confines the production of exosomes that carry cytokines such as angiopoietin-2 and proteases such as cathepsin-D. At the molecular level, CD151 docks valosin-containing protein (VCP)/p97, which controls protein quality via mediating deubiquitination for proteolytic degradation, onto endolysosomes to facilitate VCP/p97 function. At the endolysosome membrane, CD151 links VCP/p97 to i) IFITM3, which regulates MVB functions, to restrain IFITM3-mediated exosomal sorting and ii) V-ATPase, which dictates endolysosome pH, to support functional assembly of V-ATPase.

Conclusions: Distinct from its canonical function in strengthening cell adhesion at cell surface, CD151 maintains endolysosome function by sustaining VCP/p97-mediated protein unfolding and turnover. By supporting protein quality control and protein degradation, CD151 prevents proteins from i) buildup in endolysosomes and ii) discharge through exosomes, to limit vascular inflammation. Also, our study conceptualizes that balance between degradation and discharge of proteins in endothelial cells determines vascular information. Thus, the IFITM3/V-ATPase-tetraspanin-VCP/p97 complexes on endolysosome, as a protein quality control and inflammation-inhibitory machinery, could be beneficial for therapeutic intervention against vascular inflammation.

Graphical Abstract

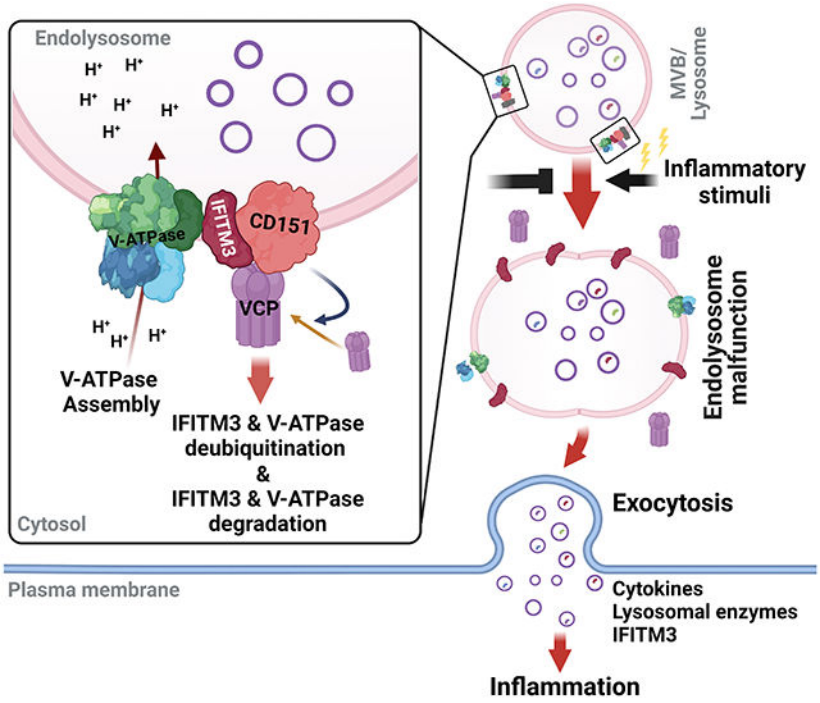

Keywords

Exosome; IFITM3; multi-vesicular body; tetraspanin-enriched membrane domain; ubiquitin; V-ATPase

Subject Terms:

Animal Models of Human Disease; Cell Signaling/Signal Transduction; Cell Biology/ Structural Biology; Inflammation; Vascular Biology

Introduction

Tetraspanin CD151, an ubiquitously expressed transmembrane protein[1], is localized at basolateral plasma membrane and in endosome/lysosome (endolysosome) and associates with laminin-binding integrins physically[2, 3]. CD151 regulates adhesion, migration, and proliferation[1] at the cellular level and kidney function, pathological angiogenesis[4] and vascular stability, thrombosis[5], and tumor progression[1] at the organismal level. Gene ablation and/or mutation of CD151 cause kidney abnormalities in mice and/or humans[6-8]. Whether CD151 affects inflammation is unknown, despite its strong presence in vasculature. The function of CD151 in endolysosomes is also unknown, despite its abundance in these vesicular compartments. CD151 also physically associates with tetraspanins such as CD9, CD63, and CD81, which are exosome markers, to form tetraspanin-enriched membrane domains (TEMD) in cell membrane[9, 10].

IFITM proteins localize largely at the endolysosome membrane, are induced by interferon, and confine viruses within endolysosome[11, 12]. For example, IFITM3 inhibits the fusion of influenza virus envelope with endolysosome limiting membrane to block the viral entry into cytoplasm for replication[13, 14]. IFITM1/Leu13 interacts with TEMD[15], but interactions of other IFITMs with TEMD remain undetermined. Notably, IFITM3 is expressed in endothelial cells (ECs)[16, 17], and its accumulation in aged brain contributes Alzheimer's disease development[18]. Whether IFITMs affect inflammation is unknown, despite their important roles in innate immunity. Endolysosomes are characterized by low pH, which is determined by V-ATPase, the proton pump localizing at the limiting membrane and consisting of multiple subunits. The role of V-ATPase in inflammation also remains unclear, although its activity directly affects master regulators for metabolism mTORC and AMPK[19].

Endolysosomes are increasingly recognized as the hubs controlling metabolism, but their contributions to inflammatory responses are still elusive. Vasculature regulates inflammatory processes by reorganizing endothelial barriers, recruiting leukocytes, and secreting cytokines. As CD151 undergoes endolysosomal trafficking[20, 21] and restrains vascular leakage[22], it situates at unique position to address if and how endolysosomes are coupled to inflammatory process. We hypothesize that CD151 maintains proper functions of endolysosomes to limit vascular inflammation. By analyzing various types of inflammation, we demonstrated i) CD151 as an anti-inflammatory regulator via sustaining endolysosome functions and ii) the protein unfolding and turnover at endolysosomal limiting membrane as inflammation-regulatory events. Also, we demonstrated that CD151 docks valosin-containing protein (VCP)/p97, which extracts proteins from multi-molecular assembly or subcellular organelle, onto endolysosomes and facilitates VCP/p97-mediated deubiquitination. Moreover, we demonstrated that CD151 i) bridges VCP/p97 interactions with IFITM3 and V-ATPase for their turnover and ii) promotes V-ATPase assembly for pH

decrease in endolysosome. Equally important, we identified IFITM3 as a TEMD component and established that IFITM3 supports inflammation by regulating the structure and function of endolysosome and the pro-inflammatory molecule sorting into exosomes.

Data availability.

The data that support the findings of this study are available from the corresponding author upon reasonable request. Detailed descriptions for all methods are provided in the Supplemental Material.

Results

Cd151 ablation in endothelia causes lung inflammation and potentiates inflammatory responses in various diseases.

To reveal the relationship of CD151 with diseases, we performed RNAseq with primary mouse lung endothelial cells (MLECs) isolated from *Cd151*$^{+/+}$ and *Cd151*$^{-/-}$ mice[22]. The Overrepresented Diseases analysis on the RNAseq data showed that *Cd151* ablation-mediated changes in gene expression associated CD151 to inflammation and inflammatory diseases (Figure S1a). In the lungs of human patients with chronic obstructive pulmonary diseases (COPD) or Covid-19, endothelial CD151 proteins were significantly decreased, compared to normal lungs (Figure S1b), and CD151 mRNA in entire lung tissue of Covid-19 patients also displayed a trend of reduction (Figure S1c). Hence, changes in endothelial CD151 expression are related to human inflammatory diseases. Moreover, inflammatory stimuli LPS, TNF-α, and IFN-γ reduced the EC surface and/or total cellular levels of CD151 (Figure S1d-e).

To assess CD151 role in vascular inflammation *in vivo*, we generated endothelial conditional *Cd151* knockout mice (*Cd151*$^{i\Delta EC}$) (Figure S2a), given the abundance of CD151 in endothelia. With specific removal of CD151 from endothelia (Figure S2b-c), *Cd151*$^{i\Delta EC}$ mice displayed disseminated pulmonary lesions at the microscopic scale, as shown by H&E staining (Figure 1a). The pathological changes appear to be progressive, given no obvious pulmonary abnormality in *Cd151*$^{i\Delta EC}$ mice at 2- and 8-weeks post-Tamoxifen administration (Figure S3a). Miles assay reported much more pronounced leakage of lung vasculature in *Cd151*$^{i\Delta EC}$ mice, compared to control (*Ctrl.*) mice, at 16 weeks, but not 2 weeks, after tamoxifen induction (Figure 1b), suggesting that *Cd151* ablation doesn't cause lung vascular leakage immediately. Staining of murine IgG deposition in perfused tissues, an established assay evaluating vascular leakage *in vivo*[23, 24], further confirmed pulmonary vascular leakage in *Cd151*$^{i\Delta EC}$ mice at 16 weeks after tamoxifen induction (Figure S3b). We also examined IgA, IgE, C3, and C1q and found no obvious accumulation of these proteins in the lungs of *Cd151*$^{i\Delta EC}$ mice (Figures 1b and S3b-d), excluding the pulmonary inflammation phenotype as the result of Ig deposition and complement activation from autoimmune response.

To follow endothelial CD151 in vascular inflammation development, we included mTmG lineage tracing model for the phenotype analysis (Figure S4a)[25]. *Cd151* ablation damaged endothelium integrity, i.e., discontinuities of endothelia, as denoted by mEGFP in

Cd151$^{i\Delta EC}$*:mTmG* and endomucin in *Cd151*$^{i\Delta EC}$ mouse lungs, compared respectively with those in *Ctrl.:mTmG* and *Ctrl.* mouse lungs (Figures 1c-d and S4b, arrows). In addition, *Cd151* ablation in endothelia caused evidently more intra- and peri-vascular cellularity (Figure 1d, arrowheads) and more infiltration of i) non-ECs or leukocytes (CD45$^+$ cells) inside and around walls of small blood vessels, ii) macrophages (F4/80$^+$ cells) in lung interstitial areas (Figure 1d), and iii) neutrophils, which are reflected by myeloperoxidase (MPO) activity (Figure 1e). Pulmonary accumulation of macrophages became detectable in *Cd151*$^{i\Delta EC}$ mice at 8 weeks, not 2 weeks, after tamoxifen injection (Figure S4c). But the levels of VCAM1, a molecule important for leukocyte recruitment, exhibited no difference between *Cd151*$^{+/+}$ and *Cd151*$^{-/-}$ MLECs (Figure S4d).

No noticeable abnormality of vasculatures was found in other organs such as liver (Figure S4e) in *Cd151*$^{i\Delta EC}$ mice at the basal level. Overall, these observations underline the integrated vascular inflammatory responses in lung upon endothelial *Cd151* removal.

We then expanded the study to inflammatory conditions or diseases. In heart, endothelial *Cd151* removal caused substantially more infiltration of inflammatory cells in myocardium, compared to control mice, in Angiotensin II (Ang II)-induced chronic inflammation (Figure 1f). During progression of the sepsis induced by bacterial endotoxin lipopolysaccharide (LPS), *Cd151*$^{i\Delta EC}$ mice displayed a significantly lower survival rate than control mice (Figures S4g and 1g). For LPS-induced acute respiratory distress syndrome (ARDS), *Cd151*$^{i\Delta EC}$ mice exhibited substantially more severe lung injury than control mice (Figure 1h). Moreover, we examined CD151 role in severe acute respiratory syndrome coronavirus 2 (SARS-CoV-2)-induced lung injury, by challenging *Cd151*$^{+/+}$;*hACE2*-tg and *Cd151*$^{-/-}$;*hACE2*-tg mice with SARS-CoV-2. *Cd151* ablation reduced animal survival and elevated weight loss only at the end (Figure 1i). More lung injury and inflammatory cell infiltration were observed in *Cd151*$^{-/-}$;*hACE2*-tg mice than in *Cd151*$^{+/+}$;*hACE2*-tg mice (Figure 1j). These results collectively indicate that endothelial *Cd151* ablation exacerbates various cardiovascular inflammations.

CD151 removal elevates endothelial production of inflammatory molecules by facilitating exosomal release.

To explore how CD151 restrains inflammation, we compared RNA-seq data from *Cd151*$^{+/+}$ and *Cd151*$^{-/-}$ MLECs and found that IL-1 and TNF pathways were the most affected signaling (Figure 2a). Analysis on cytokine secretomes of the MLEC culture supernatants revealed that IL-1β was unchanged, TNFα elevated, but angiopoietin-2 (ANGPT2) dramatically increased upon *Cd151* ablation (Figures 2b and S5a). In blood plasma of *Cd151*$^{i\Delta EC}$ mice, only ANGPT2, neither TNF-α nor IL-1β, was significantly increased, compared to those in control mice (Figures 2b and S5b). More ANGPT2 proteins were detected in the endothelium and interstitium of *Cd151*$^{i\Delta EC}$ lung (Figure 2c). Since ANGPT2 is the only cytokine that was consistently altered in *Cd151*$^{-/-}$ MLECs and *Cd151*$^{i\Delta EC}$ mice, we focused on ANGPT2 in the following studies.

Interestingly, the exosomes released by *Cd151*$^{-/-}$ MLECs carried more ANGPT2 proteins (Figure 2d). Moreover, *Cd151*$^{-/-}$ MLECs released more but smaller extracellular vesicles (EVs) than *Cd151*$^{+/+}$ MLECs, and the changes in EVs from *Cd151*$^{-/-}$ MLECs mainly

resulted from exosomes (<200 nm), not from microvesicles (>200 nm) (Figures 2e and s5c). Exosomes from *Cd151*$^{-/-}$ MLECs also displayed larger heterogeneity or irregularity in morphology (Figure 2e). CD151 knockdown in human dermal microvascular ECs (HMEC), bEnd.3 murine brain ECs, and HT1080 fibroblastoma cells reduced EV size but didn't alter EV number (Figure S5d).

Consistently, condition media of *Cd151*$^{-/-}$ MLECs markedly disrupted the barrier function of *Cd151*$^{+/+}$ MLEC monolayer, and ANGPT2 largely pheno-copied effect of the condition media (Figure 2f), suggesting that endothelial barrier-disruptive soluble factor(s) from *Cd151*$^{-/-}$ MLECs is attributed largely to ANGPT2.

As multi-vesicular bodies (MVBs) undergo exocytosis to release exosomes, we then examined MVBs and found substantial accumulation of ANGPT2 within MVBs in CD151-silenced HMECs, evidenced by elevated colocalization of ANGPT2 with lysobisphosphatidic acid (LBPA), a MVB marker (Figure 2g), indicating more ANGPT2 trafficking into MVBs.

We then applied exocytosis inhibitor Nexinhib 20 (Nex20) (5 μM)[26] to block exosome release. Nex20 abrogated or diminished *Cd151* ablation-induced increases in i) EV production (Figure 2h), ii) exosomal release of ANGPT2 (Figure 2h), and iii) endothelial secretion of ANGPT2 (Figure 2i). *In vivo*, Nex20 reduced LPS-induced lung injury and abrogated the difference between control and *Cd151*$^{i\Delta EC}$ mice (Figure 2j), indicating exocytosis inhibition rescues *Cd151* removal-aggravated lung injury. Nex20 also diminished the difference in pulmonary infiltration of neutrophils, reflected by MPO activity, between the two groups (Figure 2k). Moreover, treatment of sepsis caused by LPS with Nex20 markedly improved survival rates of the mice and largely eliminated survival difference between control and *Cd151*$^{i\Delta EC}$ groups (Figure 2l). Furthermore, ANGPT2-neutralizing antibody reduced LPS-induced lung injury in both control and *Cd151*$^{i\Delta EC}$ groups and abolished the difference between the two groups (Figure 2m and S5e). Thus, *Cd151* ablation upregulates exocytosis, leading to increased EV release of ANGPT2 and exacerbated inflammation.

CD151 removal facilitates exosomal release by upregulating IFITM3.

To identify molecular partners crucial for CD151-regulated vesicular trafficking, we searched the proteins that physically associated with CD151-integrin α3β1 complex using proteomics analysis. IFITM3, IFITM2, and Tspan14 were the novel candidates among high-score readouts, in addition to those earlier reported partners (Figure 3a). Because CD151 and IFITMs were both involved in endolysosomal trafficking[11, 20, 27], we focused on IFITMs. CD151-IFITM3 association was confirmed by co-immunoprecipitation under both 1% Brij98 and 1% Triton-X100 lysis conditions (Figure 3b) and by PLA (Figure 3c). CD151 palmitoylation-deficient mutant largely diminished physical association with IFITM3 (Figures 3d and S6a-b), indicating importance of CD151 lipidation for this association. The CD151-IFITM3 complex was further supported by their colocalization by immunofluorescence (Figure 3e).

IFITM3 protein, not IFITM1, was increased upon *Cd151* ablation (Figure 3f), and their expressions were upregulated by pro-inflammatory stimulus (Figure S6c-d) in contrast to the downregulation of CD151 (Figure S1d-e). IFN-γ and LPS treatments increased CD151-IFITM3 colocalization (Figure S6e). *Cd151* ablation or silencing enlarged IFITM3-containing vesicles and MVBs, enhanced IFITM3-LBPA co-localization, but unaltered MVB level (Figures 3g, S2e, and S6f). Super-resolution imaging analysis showed that IFITM3 and LBPA were distributed at both peripheral and intraluminal areas of MVBs in Mock group, but IFITM3 became accumulated in the peripheral area of MVBs in CD151-silenced group (Figures 3h and S6g), suggesting that CD151 supports sorting of IFITM3 from limiting membrane into intraluminal vesicle (ILV) or restricts reverse sorting of IFITM3 or ILV-limiting membrane fusion. CD151 removal also enhanced lysosomal presence of IFITM3 and enlarged lysosomes (Figure S6h). Hence, CD151 confines sizes of endolysosomes and prevents IFITM3 from accumulation in endolysosomes, especially in MVB limiting membrane.

Exosomal discharge of IFITM3 was increased in bEnd.3, MLEC, and HT1080 cells upon CD151 knockdown, so was cathepsin-D, a lysosomal protease (Figures 3i and S6i). In *Cd151*$^{i\Delta EC}$ lung vasculature, especially vessels with intermediate size, cathepsin-D deposition was significantly increased in medium, but not within endothelium (Figure 3j), implying that endothelial ablation of *Cd151* creates inflammation-prone microenvironment in vessel wall.

Despite lowering CD151 (Figure S7a), IFITM3 knockdown abolished or diminished CD151 removal-induced i) increase in exosomal release of ANGPT2 (Figure 3k), ii) upsurge of EV release (Figures 3l and S7b), and iii) decrease in EV size (Figure 3l), highlighting that CD151 restrains secretion of EVs and ANGPT2 by confining IFITM3 level. *In vivo* inhibition of IFITM3 with its down-regulator cyclosporin-H (CsH)[28] prolonged the survival of mice with LPS-caused sepsis and abrogated the difference in survival rate between *Cd151*$^{i\Delta EC}$ and *Ctrl.* mice (Figures 3m and S7c-d), suggesting that IFITM3 potentiates systemic inflammation and counteracts CD151-mediated restraint of inflammation. Moreover, AAV2^{QuadYF}-mediated *in vivo* delivery of IFITM3 shRNA to endothelia markedly reduced LPS-caused inflammatory injury and macrophage infiltration of lung and abolished or diminished the differences between the two groups (Figures 3n-o and S7e-g). Therefore, CD151 interacts with IFITM3 physically and confines its level, to restrain MVB size and exosome release for less inflammation.

To affirm an essential role of IFITM3 in CD151 function *in vivo*, we crossed *Ifitm3*$^{-/-}$ mice with *Cd151*$^{\Delta EC}$ mice but failed in generating *Cd151*$^{\Delta EC}$;*Ifitm3*$^{-/-}$ mice after examining 112 F1 pups. This failure is likely due to close adjacency of these two genes in the same chromosome (*Cd151*: Chr 7:141.05–141.05; *Ifitm3*: Chr 7:140.59–140.59). Such gene juxtaposition may reflect their functional linkage.

CD151 removal upregulates IFITM3 and its ubiquitination by dissociating VCP/p97 from endolysosomes.

Valosin-containing protein (VCP)/p97 is a member of AAA-ATPase family and directly regulates lysosomal trafficking and turnover of IFITM3[29]. We determined VCP role

in CD151-IFITM3 interactions. Notably, CD151 was colocalized with VCP, and this colocalization was largely disrupted by inflammatory stimulus LPS (Figures 4a and S8a). Neither CD151 nor IFITM3 knockdown changed VCP protein level; but CD151 formed complex with VCP, in an IFITM3-independent manner as IFITM3 knockdown didn't alter this association (Figure 4b). Atomistic molecular dynamics analysis on CD151 and VCP supports their direct association, which is stabilized, in part, by a positively charged patch formed by the cytoplasmic tails and loop of CD151 and a negatively charged patch adjacent to the N-terminal binding cleft of VCP (Figure 4c). CD151 palmitoylation, which occurs at multiple cysteine residues near the interface between inner leaflet and cytosol, is required for CD151-VCP association (Figures 3d and S6b). CD151 association with VCP was independent of p47 and Npl4, major cofactors of VCP[30], but appeared to accommodate Ufd1, another major cofactor of VCP (Figure 4d). CD151 was not required for VCP associations with p47, Npl4, and Ufd1 but confined Ufd1 level (Figure S8b). Moreover, reciprocal co-immunoprecipitation and PLA revealed the physical association between IFITM3 and VCP (Figure 4e-f). As expected, VCP and IFITM3 were colocalized, while CD151 silencing decreased this co-localization (Figures 4g and S8c) despite increased IFITM3 levels upon CD151 removal (Figure S8d-e). Also, IFITM3-VCP association was markedly reduced upon CD151 removal, as shown by both co-immunoprecipitation and PLA (Figures 4h-i and S8f), underlining CD151 intermediates the IFITM3-VCP association.

As VCP extracts and unfolds ubiquitinated IFITM3 for de-ubiquitination and subsequent degradation[29], we examined IFITM3 ubiquitination and found CD151 removal increased IFITM3 ubiquitination (Figure 4j), suggesting that CD151 anchors VCP onto MVB/lysosome and bridges VCP to IFITM3 for the IFITM3 de-ubiquitination (Figure 4k). Indeed, coalescence of VCP to MVBs, based on the VCP-LBPA co-localization, became diminished upon CD151 removal or VCP inhibitor ML240 treatment (Figure 4l); while CD151 localization to MVB was not altered by ML240 (Figure S8g), as anticipated. Similar to CD151 removal, ML240 treatment upregulated IFITM3 level (Figure 4m), supporting the notion that VCP promotes IFITM3 turnover. ML240 also enhanced IFITM3-CD151 colocalization (Figure S8h), underpinning the connection of CD151 to the IFITM3 buildup resulting from VCP inhibition. Total ubiquitination level of cellular proteins was also increased upon CD151 silencing (Figure S8i), suggesting general importance of CD151 in mediating protein deubiquitylation.

ML240 elevated EV and exosome productions in Mock and/or CD151 KD cells, and diminished or abrogated their difference in EV or exosome production, respectively (Figure 4n). In addition, ML240 enhanced IFITM3 expression and enlarged IFITM3-containing vesicles in Mock and CD151KD cells to equivalent levels (Figure 4o). In conclusion, CD151 bridges VCP-IFITM3 association by docking VCP to MVB/lysosome and prevents IFITM3 from accumulation in MVB/lysosome by maintaining VCP-mediated deubiquitination and then proteolytic degradation.

CD151 removal impairs endolysosome structure and function via VCP/p97 and IFITM3.

Both proteomics and genomics analyses underscore the relevance of lysosome and EV to CD151 functions (Figures 5a and S9). Indeed, CD151 removal increased i) number of ILVs

(Figure 5b), i.e., exosome precursors, and ii) size of MVBs (Figures 5c-e, 3g, 4l, S6f, and S10a), despite no impact on MVB quantity (Figure 3g). IFITM3 silencing reversed the MVB enlargement induced by CD151 knockdown, and IFITM3 inhibition with CsH (2.5 μM[28]) (Figure S7d) partially reversed the enlargement (Figure 5d-e), indicating IFITM3 importance in the MVB aberrancy resulting from CD151 silencing. In contrast, VCP inhibitor ML240 enlarged MVBs in both Mock and CD151 KD cells but diminished the difference in MVB size between the two groups (Figure 5d). Interestingly, LPS enhanced MVB localization of CD151(Figure S10b).

For lysosomes, CD151 silencing not only enlarged their size (Figures 5e-f and S10a), which was fully corrected by IFITM3 silencing (Figure 5e), but also decreased their numbers (Figure 5g). Besides cell-cell contact distribution (Figure S10d), CD151 is also present in lysosomes (Figure S10c), its effects on lysosomes are likely to be direct. For lysosomal function, CD151 knockdown elevated endolysosome pH (Figure 5h), implying compromised function of degradation and subsequent discharge of incompletely digested contents. Besides elevating lysosomal pH (Figures 5i and S10e), inhibitions of lysosomal proton pump/V-ATPase with bafilomycin A1 and/or VCP with ML240 also eliminated the differences in pH (Figure 5i) and size (Figure 5j) between two groups, suggesting that less VCP function contributes to higher endolysosomal pH and larger endolysosomal size in CD151-silenced cells.

Compromised lysosomal function due to CD151 removal was also reflected by cellular accumulation of the proteins that undergo lysosomal degradation such as insulin receptor (INSR)[31], amyloid precursor protein (APP)[32], and sequestosome-1 (SQSTM1)[33] (Figure 5k). Using purified lysosomes, we confirmed IFITM3 was also accumulated in the lysosomes upon CD151 removal (Figure 5l), further supporting dysfunctional lysosomes in CD151-removed ECs.

CD151 removal compromises the assembly of V-ATPase complex.

Because of the change in pH, we examined V-ATPase, the proton pump determining endolysosomal pH. Transmembrane ATPV0B and cytosolic ATPV1A subunits of V-ATPase were upregulated upon CD151 KO and/or KD (Figures 6a). In addition, lysosomal coalescence of ATP6V1A was markedly decreased (Figures 6b) while ubiquitination of ATP6V1A was increased, by either CD151 silencing or ML240 treatment (Figure 6c). Physical interactions between V0 and V1 subunits and between V0 subunits were diminished upon CD151 silencing (Figures 6d-e), indicating that CD151 is required for proper assembly of V-ATPase. IFITM3 was reported to regulate lysosomal pH[34, 35] through physical interaction with V-ATPase[36]. Indeed, IFITM3 associated with ATP6V1A, evidenced by co-IP and PLA analyses (Figures 6f and S10f). CD151 removal also markedly reduced IFITM3 associations with the V1 and V0 subunits (Figure 6f). Although IFITM3 silencing didn’t change protein levels of V-ATPase subunits (Figure S10g), the association between V1 and V0 subunits was diminished (Figure 6g), suggesting that IFITM3 is also needed for proper V-ATPase assembly.

As VCP inhibitor ML240 enlarges endolysosome, these observations collectively underscore the necessity of VCP-CD151-IFITM3 complex for assembling V-ATPase machinery to

lower endolysosomal pH (Figure 6h). Taken together, VCP-CD151-IFITM3 complex sustains structural and functional integrity of MVBs/lysosomes.

Furthermore, inflammatory stimuli reduced CD151 level, enhanced IFITM3 and IFITM1 levels, but unaltered VCP level (Figures S1d-e and S6c-d), supporting a contrasting role of CD151 and IFITM3 in inflammatory response. In addition, IFITM3 knockdown did not change CD151 protein level (Figure S10h). At the transcriptional level (Figure S11), the majority of these genes are generally positively correlated (red color) with one another across multiple experiments, both in overall tissues (Upper panel) and even more so in endothelial tissues (Lower panel). While a smaller set are generally correlated with each other but anti-correlated (green) with the larger set.

Collectively, CD151 is an inhibitor of vascular inflammation and directly supports the formations of VCP-IFITM3 and IFITM3-V-ATPase complexes, to i) confine IFITM3 level for less pro-inflammatory exosomal release and ii) support V-ATPase assembly for proper endolysosomal functions (Figures 6i and S12). CD151 constitutes protein quality control machinery with VCP by docking VCP onto endolysosomes and supporting VCP activity, to maintain and balance the lysosomal degradation and exosomal discharge functions of cells.

Discussion

Our study reveals that CD151 restrains exosomal release of pro-inflammatory cytokines and proteases by sustaining structural and functional integrity of MVB/lysosome, to suppress acute or chronic and local or systemic vascular inflammations. Our study also reveals that CD151 regulates protein quality control in MVB/lysosome, transforming the conventional view on CD151 as a cell adhesion-regulatory protein. Our study further reveals that CD151 anchors VCP onto MVB/lysosome, to facilitate the i) degradation of ubiquitinated IFITM3 and V-ATPase subunit(s), ii) proper formation of ILV, and iii) assembly of V-ATPase, for sound MVB/lysosomal function and less pro-inflammatory exosomal discharge. Hence, CD151 in endolysosome serves as not only a component of the machinery for protein quality control but also a molecular switch for endolysosome functions.

At the organism level, CD151 regulates tumor progression[1], renal function, fibrosis[37], and pathological angiogenesis. At the cellular level, CD151 promotes cell adhesion and migration by interacting with laminin-binding integrins. Our study demonstrates that endothelial ablation of *Cd151* in mice after birth leads to chronic inflammation of blood vessels. CD151 also exhibits protective roles against inflammatory challenges like LPS and SARS-Cov-2. Mechanistically, aberrant structure and function of MVB/lysosome due to i) *Cd151* removal, ii) VCP disengagement, iii) IFITM3 accumulation, and iv) V-ATPase mis-assembly cause increased endothelial secretion and vascular deposition of cytokines and proteases and subsequently vascular inflammation.

Crosstalk of EC adhesion with endolysosome regulates inflammation.

In contrast to the earlier observation that EC interaction with matrix protein fibronectin provokes inflammation[38], we found that EC interaction with matrix protein laminin, which

is mediated by CD151-associated laminin-binding integrins and strengthened by CD151[22, 39, 40], prevents inflammation. Hence, EC-laminin interaction has inflammation-preventive or -inhibitory function, departing from traditional view on EC adhesion onto matrix as simply an anchorage mechanism for endothelia.

Beyond the established understanding that EC-matrix adhesion supports EC-EC adhesion and then endothelial barrier function to avoid inflammation, our findings also suggest that CD151-reinforced EC-matrix adhesion coordinates with MVB/lysosome to limit endothelial production of pro-inflammatory exosomes and then avoid inflammation. More importantly, our study demonstrates that the presence of CD151 in MVB/lysosome directly sets a low inflammatory status (see below) for the cells and their microenvironment, in addition to its presence at the plasma membrane for enhancing EC-matrix adhesion. Hence, departing from the canonical function of CD151 as a cell adhesion enhancer, we reveal a non-canonical function of CD151, facilitating protein quality control or protein turnover in endolysosomes (Figure S12).

CD151 coupling with VCP-IFITM3/V-ATPase complexes maintain MVB/lysosome structure and function but confine exosome production.

MVB/lysosome aberrancies in CD151-removed cells, including less acidification, size enlargement, and number diminution, indicate CD151 necessity for proper structures and functions of MVB/lysosome. Although the in-depth mechanism(s) remains to be further delineated, CD151 supports MVB/lysosome by docking VCP to limit IFITM3 level and promote V-APTase assembly. VCP unfolds ubiquitinated proteins for proteolytic degradation. Interestingly, VCP anchors to ER via derlin, a tetraspanin-like 4-transmembrane protein, for retro-translocation, ubiquitination, and ER-associated degradation (ERAD) of proteins[41, 42]. VCP function at endolysosomes is not well-understood[43], while our study shows that, with the support of CD151, VCP mediates endosome/lysosome-associated degradation (ELAD) of IFITM3, V1A subunit of V-ATPase, and likely other limiting membrane proteins, to maintain i) proper trafficking and function of endolysosomes and ii) proper formation of ILVs and then exosome. Hence, similar to derlin anchorage of VCP to ER for ERAD to alleviate ER stress, CD151 anchors VCP to endolysosome for ELAD to alleviate endolysosomal stress.

MVBs fuse with either plasma membrane for exosome release or lysosome for cargo degradation. Inhibition of lysosome increases the discharge of cargos via exosomes[44-46] and the release of exosomes by exocytosis[46-49]. CD151 regulates exosome quantitatively and qualitatively. Increase in exosome production in primary *Cd151-null* ECs may not be a cell-autonomous effect, as the change was not observed in CD151-silenced cells; but decrease in exosome size and alteration in exosome component exist in all CD151-removed cells and likely result from accumulated IFITM3 in MVB limiting membrane. In CD151-removed cells, incomplete proteolysis due to i) higher pH caused by dysfunctional V-ATPases and/or ii) aberrant sorting into ILVs caused by IFITM3 buildup can lead to more release of exosome-carrying cytokines and proteases.

IFITM3 helps acidify endolysosomes[34, 50] and form ILVs[13, 50, 51]. CD151 limits ILV formation and exosome production likely by confining IFITM3 ubiquitination and then its

level in MVB/lysosome. Indeed, IFITM3 silencing or inhibition ameliorates *in vitro* and *in vivo* phenotypes caused by CD151 removal. Notably, IFITM3 function in MVB requires its interaction with PIP3 through its intact, cytosol-facing lysine residues[52], while excessive ubiquitination of IFITM3, as seen in CD151-removed cells, may impede and block this interaction and thereby compromise IFITM3 function. As pathophysiological functions of IFITM3 are expanded from earlier established preventive roles in the infection of enveloped viruses to newly discovered promotive roles in Alzheimer's disease and B-cell leukemia[12, 18, 53], our finding of CD151 as a crucial partner for IFITM3 prompts future studies on the link of CD151 to these diseases.

Exosomal discharge of pro-inflammatory molecules upon endothelial CD151 removal

ANGPT2 released by ECs can cause endothelial barrier dysfunction and inflammation[54]. Inflammatory phenotypes of endothelial *Cd151* ablation are attributed largely to ANGPT2, although the contribution of cathepsin-D remains to be determined. The phenotypes are attenuated substantially by inhibition of exosomal exocytosis, underlining that CD151 prevents vascular inflammation by restraining exosome-mediated release of cytokines and proteases. Inhibition of exosomal release also reduces LPS-induced inflammation even when CD151 is present (Figure 2j-l), so does blockade of ANGPT2 (Figure 2m), suggesting their general importance in vascular inflammation.

Exosomal presence and release of ANGPT2, based on the lines of observations from this study, are not contradictory to the tradition view of ANGPT2 presence in and release from Weibel-Palade body in endothelial cells[55]. First, other residents and/or markers of Weibel-Palade body such as P-selectin and CD63 are also present in MVB and traffic between Weibel-Palade body and late endosomes such as MVB[56, 57]. Second, Weibel-Palade body can also form and discharge ILV[58]. Hence, some exosomes from ECs may originate directly from Weibel-Palade body. Moreover, exosomal releases of ANGPT2, other angiopoietins, and angiopoietin-like proteins by various cells including ECs have been reported[59-61], although those studies didn't reveal the subcellular compartment from which the ANGPT2-carrying exosomes are derived. In CD151-removed ECs, dysfunctional lysosomes may not fully degrade internalized ANGPT2, leading to more exosomal release of ANGPT2 from MVBs for recycled or extended ANGPT2 activity. This possibility could explain the potency or prominence of ANGPT2 in inflammation models in this study.

For TNF-α, although it is not elevated in the blood of $Cd151^{\Delta EC}$ mice and thereby not responsible for their phenotypes, increased production of TNF-α by ECs could also attribute to the more exosomes upon CD151 removal as exosomes mediate TNF-α release in ECs[62, 63].

CD151, IFITM3, and VCP/p97 as inflammation regulators for therapeutic benefits

CD151 physically associates with IFITM3, which is localized mainly in endolysosome. Upon *Cd151* ablation, more IFITM3 are accumulated in MVBs/lysosomes, leading to aberrant MVB/lysosome functions and then increased exocytosis. IFITM3 affects cellular entry, endosomal fusion, and inter-cellular dissemination of various enveloped viruses[64], and

our observation of IFITM3 as an inflammation amplifier reveals not only its unknown role in inflammation but also its potential as a therapeutic target against inflammation.

CD151 prevents but IFITM3 supports exosomal release, probably also sorting, of cytokines and proteases, which exacerbate inflammation. Given their accessibility at cell surface, CD151 and IFITM3 can be regulated for their levels for therapeutic purposes. Together with aforementioned anti-inflammation merits of endothelial CD151, these unique features place CD151 in a promising position for clinical prevention and treatment of vascular inflammation and inflammatory diseases in future.

In conclusion, by forming protein quality control machinery with VCP/p97, CD151 maintains protein quality, facilitates protein turnover, and determines the protein turnover routes (proteolytic degradation versus exosomal discharge) at the limiting membrane of endolysosomes, to support the structural and functional integrity of endolysosomes, restrain cellular inflammatory response, and subsequently inhibit vascular inflammation (Figure S12). Without exogenous challenge, endothelial *Cd151* ablation appears to affect mouse lung selectively. Such selectivity results unlikely from differential expression of CD151 in vasculature of different organs, given CD151 abundance in almost all endothelia[65], but possibly from endothelium property and mechanical environment of different vascular beds. Also, how exosomal discharge of pro-inflammatory molecules from *Cd151-null* ECs leads to pulmonary infiltration of leukocytes is unclear. These unanswered questions warrant further mechanistic analysis in future studies.

Supplementary Material

Refer to Web version on PubMed Central for supplementary material.

Acknowledgements

We thank OMRF Cardiovascular Biology Research Program for discussions.

Sources of Funding

This work was supported by NIH grants HL132553, HL137819, and GM135547 and AHA grants 13GRNT17040028 and 15GRNT25700426 to XAZ. The core facilities were supported by NIH grants P20GM103639 and P30CA225520.

Non-standard Abbreviations and Acronyms

AAA-ATPase	ATPases Associated with Diverse Cellular Activity
AAV2	Adeno-associated virus type 2
ANGPT2	Angiopoietin-2
APP	Amyloid precursor protein
ARDS	Acute respiratory distress syndrome
COPD	Chronic obstructive pulmonary diseases

CoV-2	Coronavirus 2
CsH	Cyclosporin-H
EC	Endothelial cell
ELAD	Endosome/lysosome-associated degradation
ER	Endoplasmic reticulum
ERAD	ER-associated degradation
EV	Extracellualr vesicle
hACE2	Human Angiotensin-converting enzyme 2
HMEC	Human microvascular endothelial cell
IFN-γ	Interferon gamma
ILV	Intraluminal vesicle
IL-1β	Interleukin 1 beta
INSR	Insulin receptor
LBPA	Lysobisphosphatidic acid
LPS	Lipopolysaccharide
mEGFP	membrane-targeted enhanced green fluorescent protein
MLEC	Mouse lung endothelial cell
MPO	Myeloperoxidase
mTmG	membrane-Tomato/membrane-Green
MVB	Multi-vesicular body
Nex20	Nexinhib 20
PLA	Proximity ligation assay
SARS	Severe acute respiratory syndrome
SQSTM1	Sequestosome-1
TEER	Trans-endothelial electrical resistance
TNF-α	Tumour necrosis factor α
TEMD	Tetraspanin-enriched membrane domains
VCP	Valosin-containing protein

References:

1. Hemler ME. Tetraspanin proteins promote multiple cancer stages. Nature Reviews Cancer. 2014;14:49–60 [PubMed: 24505619]
2. Kazarov AR, Yang X, Stipp CS, Sehgal B, Hemler ME. An extracellular site on tetraspanin cd151 determines alpha 3 and alpha 6 integrin-dependent cellular morphology. The Journal of cell biology. 2002;158:1299–1309 [PubMed: 12356873]
3. Sterk LM, Geuijen CA, van den Berg JG, Claessen N, Weening JJ, Sonnenberg A. Association of the tetraspanin cd151 with the laminin-binding integrins alpha3beta1, alpha6beta1, alpha6beta4 and alpha7beta1 in cells in culture and in vivo. Journal of cell science. 2002;115:1161–1173 [PubMed: 11884516]
4. Takeda Y, Kazarov AR, Butterfield CE, Hopkins BD, Benjamin LE, Kaipainen A, Hemler ME. Deletion of tetraspanin cd151 results in decreased pathologic angiogenesis in vivo and in vitro. Blood. 2007;109:1524–1532 [PubMed: 17023588]
5. Orlowski E, Chand R, Yip J, Wong C, Goschnick MW, Wright MD, Ashman LK, Jackson DE. A platelet tetraspanin superfamily member, cd151, is required for regulation of thrombus growth and stability in vivo. Journal of thrombosis and haemostasis : JTH. 2009;7:2074–2084 [PubMed: 19740096]
6. Baleato RM, Guthrie PL, Gubler MC, Ashman LK, Roselli S. Deletion of cd151 results in a strain-dependent glomerular disease due to severe alterations of the glomerular basement membrane. The American journal of pathology. 2008;173:927–937 [PubMed: 18787104]
7. Sachs N, Claessen N, Aten J, Kreft M, Teske GJ, Koeman A, Zuurbier CJ, Janssen H, Sonnenberg A. Blood pressure influences end-stage renal disease of cd151 knockout mice. The Journal of clinical investigation. 2012;122:348–358 [PubMed: 22201679]
8. Karamatic Crew V, Burton N, Kagan A, Green CA, Levene C, Flinter F, Brady RL, Daniels G, Anstee DJ. Cd151, the first member of the tetraspanin (tm4) superfamily detected on erythrocytes, is essential for the correct assembly of human basement membranes in kidney and skin. Blood. 2004;104:2217–2223 [PubMed: 15265795]
9. Charrin S, Jouannet S, Boucheix C, Rubinstein E. Tetraspanins at a glance. Journal of cell science. 2014;127:3641–3648 [PubMed: 25128561]
10. Yanez-Mo M, Barreiro O, Gordon-Alonso M, Sala-Valdes M, Sanchez-Madrid F. Tetraspanin-enriched microdomains: A functional unit in cell plasma membranes. Trends in cell biology. 2009;19:434–446 [PubMed: 19709882]
11. Diamond MS, Farzan M. The broad-spectrum antiviral functions of ifit and ifitm proteins. Nature reviews. Immunology. 2013;13:46–57
12. Brass AL, Huang IC, Benita Y, John SP, Krishnan MN, Feeley EM, Ryan BJ, Weyer JL, van der Weyden L, Fikrig E, Adams DJ, Xavier RJ, Farzan M, Elledge SJ. The ifitm proteins mediate cellular resistance to influenza a h1n1 virus, west nile virus, and dengue virus. Cell. 2009;139:1243–1254 [PubMed: 20064371]
13. Feeley EM, Sims JS, John SP, Chin CR, Pertel T, Chen LM, Gaiha GD, Ryan BJ, Donis RO, Elledge SJ, Brass AL. Ifitm3 inhibits influenza a virus infection by preventing cytosolic entry. PLoS pathogens. 2011;7
14. Li K, Markosyan RM, Zheng YM, Golfetto O, Bungart B, Li M, Ding S, He Y, Liang C, Lee JC, Gratton E, Cohen FS, Liu SL. Ifitm proteins restrict viral membrane hemifusion. PLoS pathogens. 2013;9:e1003124 [PubMed: 23358889]
15. Takahashi S, Doss C, Levy S, Levy R. Tapa-1, the target of an antiproliferative antibody, is associated on the cell surface with the leu-13 antigen. Journal of immunology (Baltimore, Md. : 1950). 1990;145:2207–2213 [PubMed: 2398277]
16. Bailey CC, Huang IC, Kam C, Farzan M. Ifitm3 limits the severity of acute influenza in mice. PLoS pathogens. 2012;8:e1002909 [PubMed: 22969429]
17. Sun X, Zeng H, Kumar A, Belser JA, Maines TR, Tumpey TM. Constitutively expressed ifitm3 protein in human endothelial cells poses an early infection block to human influenza viruses. Journal of virology. 2016;90:11157–11167 [PubMed: 27707929]

18. Hur JY, Frost GR, Wu X, Crump C, Pan SJ, Wong E, Barros M, Li T, Nie P, Zhai Y, Wang JC, Tcw J, Guo L, McKenzie A, Ming C, Zhou X, Wang M, Sagi Y, Renton AE, Esposito BT, Kim Y, Sadleir KR, Trinh I, Rissman RA, Vassar R, Zhang B, Johnson DS, Masliah E, Greengard P, Goate A, Li YM. The innate immunity protein ifitm3 modulates gamma-secretase in alzheimer's disease. Nature. 2020;586:735–740 [PubMed: 32879487]
19. Zhang CS, Jiang B, Li M, Zhu M, Peng Y, Zhang YL, Wu YQ, Li TY, Liang Y, Lu Z, Lian G, Liu Q, Guo H, Yin Z, Ye Z, Han J, Wu JW, Yin H, Lin SY, Lin SC. The lysosomal v-atpase-ragulator complex is a common activator for ampk and mtorc1, acting as a switch between catabolism and anabolism. Cell metabolism. 2014;20:526–540 [PubMed: 25002183]
20. Sincock PM, Fitter S, Parton RG, Berndt MC, Gamble JR, Ashman LK. Peta-3/cd151, a member of the transmembrane 4 superfamily, is localised to the plasma membrane and endocytic system of endothelial cells, associates with multiple integrins and modulates cell function. Journal of cell science. 1999;112 (Pt 6):833–844 [PubMed: 10036233]
21. Liu L, He B, Liu WM, Zhou D, Cox JV, Zhang XA. Tetraspanin cd151 promotes cell migration by regulating integrin trafficking. The Journal of biological chemistry. 2007;282:31631–31642 [PubMed: 17716972]
22. Zhang F, Michaelson JE, Moshiach S, Sachs N, Zhao W, Sun Y, Sonnenberg A, Lahti JM, Huang H, Zhang XA. Tetraspanin cd151 maintains vascular stability by balancing the forces of cell adhesion and cytoskeletal tension. Blood. 2011;118:4274–4284 [PubMed: 21832275]
23. Shindo A, Maki T, Mandeville ET, Liang AC, Egawa N, Itoh K, Itoh N, Borlongan M, Holder JC, Chuang TT, McNeish JD, Tomimoto H, Lok J, Lo EH, Arai K. Astrocyte-derived pentraxin 3 supports blood-brain barrier integrity under acute phase of stroke. Stroke. 2016;47:1094–1100 [PubMed: 26965847]
24. Oshima T, Laroux FS, Coe LL, Morise Z, Kawachi S, Bauer P, Grisham MB, Specian RD, Carter P, Jennings S, Granger DN, Joh T, Alexander JS. Interferon-gamma and interleukin-10 reciprocally regulate endothelial junction integrity and barrier function. Microvascular research. 2001;61:130–143 [PubMed: 11162203]
25. Muzumdar MD, Tasic B, Miyamichi K, Li L, Luo L. A global double-fluorescent cre reporter mouse. Genesis. 2007;45:593–605 [PubMed: 17868096]
26. Johnson JL, Ramadass M, He J, Brown SJ, Zhang J, Abgaryan L, Biris N, Gavathiotis E, Rosen H, Catz SD. Identification of neutrophil exocytosis inhibitors (nexinhibs), small molecule inhibitors of neutrophil exocytosis and inflammation: Druggability of the small gtpase rab27a. The Journal of biological chemistry. 2016;291:25965–25982 [PubMed: 27702998]
27. Yánez DC, Ross S, Crompton T. The ifitm protein family in adaptive immunity. 2020;159:365–372
28. Petrillo C, Thorne LG, Unali G, Schiroli G, Giordano AMS, Piras F, Cuccovillo I, Petit SJ, Ahsan F, Noursadeghi M, Clare S, Genovese P, Gentner B, Naldini L, Towers GJ, Kajaste-Rudnitski A. Cyclosporine h overcomes innate immune restrictions to improve lentiviral transduction and gene editing in human hematopoietic stem cells. Cell stem cell. 2018;23:820–832 e829 [PubMed: 30416070]
29. Wu X, Spence JS, Das T, Yuan X, Chen C, Zhang Y, Li Y, Sun Y, Chandran K, Hang HC, Peng T. Site-specific photo-crosslinking proteomics reveal regulation of ifitm3 trafficking and turnover by vcp/p97 atpase. Cell chemical biology. 2020;27:571–585 e576 [PubMed: 32243810]
30. Meyer H, Bug M, Bremer S. Emerging functions of the vcp/p97 aaa-atpase in the ubiquitin system. Nature cell biology. 2012;14:117–123 [PubMed: 22298039]
31. Iraburu MJ, Garner T, Montiel-Duarte C. Revising endosomal trafficking under insulin receptor activation. International journal of molecular sciences. 2021;22
32. Miranda AM, Lasiecka ZM, Xu Y, Neufeld J, Shahriar S, Simoes S, Chan RB, Oliveira TG, Small SA, Di Paolo G. Neuronal lysosomal dysfunction releases exosomes harboring app c-terminal fragments and unique lipid signatures. Nature communications. 2018;9:291
33. Yang L, Ying S, Hu S, Zhao X, Li M, Chen M, Zhu Y, Song P, Zhu L, Jiang T, An H, Yousafzai NA, Xu W, Zhang Z, Wang X, Feng L, Jin H. Egfr tkis impair lysosome-dependent degradation of sqstm1 to compromise the effectiveness in lung cancer. Signal transduction and targeted therapy. 2019;4:25 [PubMed: 31637005]

34. Shi GL, Schwartz O, Compton AA. More than meets the i: The diverse antiviral and cellular functions of interferon-induced transmembrane proteins. Retrovirology. 2017;14
35. Zhang H, Zoued A, Liu X, Sit B, Waldor MK. Type i interferon remodels lysosome function and modifies intestinal epithelial defense. Proceedings of the National Academy of Sciences of the United States of America. 2020;117:29862–29871 [PubMed: 33172989]
36. Wee YS, Roundy KM, Weis JJ, Weis JH. Interferon-inducible transmembrane proteins of the innate immune response act as membrane organizers by influencing clathrin and v-atpase localization and function. Innate immunity. 2012;18:834–845 [PubMed: 22467717]
37. Tsujino K, Takeda Y, Arai T, Shintani Y, Inagaki R, Saiga H, Iwasaki T, Tetsumoto S, Jin Y, Ihara S, Minami T, Suzuki M, Nagatomo I, Inoue K, Kida H, Kijima T, Ito M, Kitaichi M, Inoue Y, Tachibana I, Takeda K, Okumura M, Hemler ME, Kumanogoh A. Tetraspanin cd151 protects against pulmonary fibrosis by maintaining epithelial integrity. American journal of respiratory and critical care medicine. 2012;186:170–180 [PubMed: 22592804]
38. Yun S, Budatha M, Dahlman JE, Coon BG, Cameron RT, Langer R, Anderson DG, Baillie G, Schwartz MA. Interaction between integrin alpha5 and pde4d regulates endothelial inflammatory signalling. Nature cell biology. 2016;18:1043–1053 [PubMed: 27595237]
39. Lammerding J, Kazarov AR, Huang H, Lee RT, Hemler ME. Tetraspanin cd151 regulates alpha6beta1 integrin adhesion strengthening. Proceedings of the National Academy of Sciences of the United States of America. 2003;100:7616–7621 [PubMed: 12805567]
40. Hynes RO, Ruoslahti E, Springer TA. Reflections on integrins-past, present, and future: The albert lasker basic medical research award. Jama. 2022;328:1291–1292 [PubMed: 36170060]
41. Ye YH, Shibata Y, Yun C, Ron D, Rapoport TA. A membrane protein complex mediates retro-translocation from the er lumen into the cytosol. Nature. 2004;429:841–847 [PubMed: 15215856]
42. Wu XD, Siggel M, Ovchinnikov S, Mi W, Svetlov V, Nudler E, Liao MF, Hummer G, Rapoport TA. Structural basis of er-associated protein degradation mediated by the hrd1 ubiquitin ligase complex. Science. 2020;368:385-+
43. van den Boom J, Meyer H. Vcp/p97-mediated unfolding as a principle in protein homeostasis and signaling. Molecular cell. 2018;69:182–194 [PubMed: 29153394]
44. Hessvik NP, verbye A, Brech A, Torgersen ML, Jakobsen IS, Sandvig K, Llorente A. Pikfyve inhibition increases exosome release and induces secretory autophagy. Cellular and Molecular Life Sciences. 2016;73:4717–4737 [PubMed: 27438886]
45. Edgar JR, Manna PT, Nishimura S, Banting G, Robinson MS. Tetherin is an exosomal tether. Elife. 2016;5
46. Villarroya-Beltri C, Baixauli F, Mittelbrunn M, Fernandez-Delgado I, Torralba D, Moreno-Gonzalo O, Baldanta S, Enrich C, Guerra S, Sanchez-Madrid F. Isgylation controls exosome secretion by promoting lysosomal degradation of mvb proteins. Nature communications. 2016;7
47. Adams SD, Csere J, D'angelo G, Carter EP, Romao M, Arnandis T, Dodel M, Kocher HM, Grose R, Raposo G, Mardakheh F, Godinho SA. Centrosome amplification mediates small extracellular vesicle secretion via lysosome disruption. Curr Biol. 2021;31:1403-+ [PubMed: 33592190]
48. van Niel G, D'Angelo G, Raposo G. Shedding light on the cell biology of extracellular vesicles. Nature reviews. Molecular cell biology. 2018;19:213–228 [PubMed: 29339798]
49. Eitan E, Suire C, Zhang S, Mattson MP. Impact of lysosome status on extracellular vesicle content and release. Ageing Res Rev. 2016;32:65–74 [PubMed: 27238186]
50. Amini-Bavil-Olyaee S, Choi YJ, Lee JH, Shi MD, Huang IC, Farzan M, Jung JU. The antiviral effector ifitm3 disrupts intracellular cholesterol homeostasis to block viral entry (vol 13, pg 452, 2013). Cell host & microbe. 2013;14:600–601
51. Benfield CTO, Smith SE, Wright E, Wash RS, Ferrara F, Temperton NJ, Kellam P. Bat and pig ifn-induced transmembrane protein 3 restrict cell entry by influenza virus and lyssaviruses. J Gen Virol. 2015;96:991–1005 [PubMed: 25614588]
52. Unali G, Crivicich G, Pagani I, Abou-Alezz M, Folchini F, Valeri E, Matafora V, Reisz JA, Giordano AMS, Cuccovillo I, Butta GM, Donnici L, D'Alessandro A, De Francesco R, Manganaro L, Cittaro D, Merelli I, Petrillo C, Bachi A, Vicenzi E, Kajaste-Rudnitski A. Interferon-inducible phospholipids govern ifitm3-dependent endosomal antiviral immunity. The EMBO journal. 2023:e112234 [PubMed: 36970857]

53. Lee J, Robinson ME, Ma N, Artadji D, Ahmed MA, Xiao G, Sadras T, Deb G, Winchester J, Cosgun KN, Geng HM, Chan LN, Kume K, Miettinen TP, Zhang Y, Nix MA, Klemm L, Chen CW, Chen JJ, Khairnar V, Wiita AP, Thomas-Tikhonenko A, Farzan M, Jung JU, Weinstock DM, Manalis SR, Diamond MS, Vaidehi N, Muschen M. Ifitm3 functions as a pip3 scaffold to amplify pi3k signalling in b cells (vol 588, pg 491, 2020). Nature. 2021;592
54. Jenny Zhou H, Qin L, Zhang H, Tang W, Ji W, He Y, Liang X, Wang Z, Yuan Q, Vortmeyer A, Toomre D, Fuh G, Yan M, Kluger MS, Wu D, Min W. Endothelial exocytosis of angiopoietin-2 resulting from ccm3 deficiency contributes to cerebral cavernous malformation. Nature medicine. 2016;22:1033–1042
55. Fiedler U, Scharpfenecker M, Koidl S, Hegen A, Grunow V, Schmidt JM, Kriz W, Thurston G, Augustin HG. The tie-2 ligand angiopoietin-2 is stored in and rapidly released upon stimulation from endothelial cell weibel-palade bodies. Blood. 2004;103:4150–4156 [PubMed: 14976056]
56. McCormack JJ, Lopes da Silva M, Ferraro F, Patella F, Cutler DF. Weibel-palade bodies at a glance. Journal of cell science. 2017;130:3611–3617 [PubMed: 29093059]
57. Kobayashi T, Vischer UM, Rosnoblet C, Lebrand C, Lindsay M, Parton RG, Kruithof EK, Gruenberg J. The tetraspanin cd63/lamp3 cycles between endocytic and secretory compartments in human endothelial cells. Molecular biology of the cell. 2000;11:1829–1843 [PubMed: 10793155]
58. Streetley J, Fonseca AV, Turner J, Kiskin NI, Knipe L, Rosenthal PB, Carter T. Stimulated release of intraluminal vesicles from weibel-palade bodies. Blood. 2019;133:2707–2717 [PubMed: 30760452]
59. Ju R, Zhuang ZW, Zhang J, Lanahan AA, Kyriakides T, Sessa WC, Simons M. Angiopoietin-2 secretion by endothelial cell exosomes: Regulation by the phosphatidylinositol 3-kinase (pi3k)/akt/endothelial nitric oxide synthase (enos) and syndecan-4/syntenin pathways. The Journal of biological chemistry. 2014;289:510–519 [PubMed: 24235146]
60. Chen L, Xiang B, Wang X, Xiang C. Exosomes derived from human menstrual blood-derived stem cells alleviate fulminant hepatic failure. Stem cell research & therapy. 2017;8:9 [PubMed: 28115012]
61. Liu J, Yan Z, Yang F, Huang Y, Yu Y, Zhou L, Sun Z, Cui D, Yan Y. Exosomes derived from human umbilical cord mesenchymal stem cells accelerate cutaneous wound healing by enhancing angiogenesis through delivering angiopoietin-2. Stem cell reviews and reports. 2021;17:305–317 [PubMed: 32613452]
62. Essandoh K, Yang L, Wang X, Huang W, Qin D, Hao J, Wang Y, Zingarelli B, Peng T, Fan GC. Blockade of exosome generation with gw4869 dampens the sepsis-induced inflammation and cardiac dysfunction. Biochimica et biophysica acta. 2015;1852:2362–2371 [PubMed: 26300484]
63. Yu X, Deng L, Wang D, Li N, Chen X, Cheng X, Yuan J, Gao X, Liao M, Wang M, Liao Y. Mechanism of tnf-alpha autocrine effects in hypoxic cardiomyocytes: Initiated by hypoxia inducible factor 1alpha, presented by exosomes. Journal of molecular and cellular cardiology. 2012;53:848–857 [PubMed: 23085511]
64. Spence JS, He R, Hoffmann HH, Das T, Thinon E, Rice CM, Peng T, Chandran K, Hang HC. Ifitm3 directly engages and shuttles incoming virus particles to lysosomes. Nature chemical biology. 2019;15:259–268 [PubMed: 30643282]
65. Sincock PM, Mayrhofer G, Ashman LK. Localization of the transmembrane 4 superfamily (tm4sf) member peta-3 (cd151) in normal human tissues: Comparison with cd9, cd63, and alpha5beta1 integrin. The journal of histochemistry and cytochemistry : official journal of the Histochemistry Society. 1997;45:515–525 [PubMed: 9111230]
66. Zevian S, Winterwood NE, Stipp CS. Structure-function analysis of tetraspanin cd151 reveals distinct requirements for tumor cell behaviors mediated by alpha3beta1 versus alpha6beta4 integrin. The Journal of biological chemistry. 2011;286:7496–7506 [PubMed: 21193415]
67. Starr ME, Ueda J, Takahashi H, Weiler H, Esmon CT, Evers BM, Saito H. Age-dependent vulnerability to endotoxemia is associated with reduction of anticoagulant factors activated protein c and thrombomodulin. Blood. 2010;115:4886–4893 [PubMed: 20348393]
68. Zhang X, Wang T, Yuan ZC, Dai LQ, Zeng N, Wang H, Liu L, Wen FQ. Mitochondrial peptides cause proinflammatory responses in the alveolar epithelium via fpr-1, mapks, and akt: A potential mechanism involved in acute lung injury. American journal of physiology. Lung cellular and molecular physiology. 2018;315:L775–L786 [PubMed: 30188748]

69. An YA, Sun K, Joffin N, Zhang F, Deng Y, Donze O, Kusminski CM, Scherer PE. Angiopoietin-2 in white adipose tissue improves metabolic homeostasis through enhanced angiogenesis. eLife. 2017;6
70. Zhuo XJ, Hao Y, Cao F, Yan SF, Li H, Wang Q, Cheng BH, Ying BY, Smith FG, Jin SW. Protectin dx increases alveolar fluid clearance in rats with lipopolysaccharide-induced acute lung injury. Experimental & molecular medicine. 2018;50:1–13
71. Ye S, Luo W, Khan ZA, Wu G, Xuan L, Shan P, Lin K, Chen T, Wang J, Hu X, Wang S, Huang W, Liang G. Celastrol attenuates angiotensin ii-induced cardiac remodeling by targeting stat3. Circulation research. 2020;126:1007–1023 [PubMed: 32098592]
72. REED LJ, MUENCH H. A simple method of estimating fifty per cent endpoints12. American Journal of Epidemiology. 1938;27:493–497
73. Wang S, Zhu G, Jiang D, Rhen J, Li X, Liu H, Lyu Y, Tsai P, Rose Y, Nguyen T, White RJ, Pryhuber GS, Mariani TJ, Li C, Mohan A, Xu Y, Pang J. Reduced notch1 cleavage promotes the development of pulmonary hypertension. Hypertension. 2022;79:79–92 [PubMed: 34739767]
74. Huang X, Dai Z, Cai L, Sun K, Cho J, Albertine KH, Malik AB, Schraufnagel DE, Zhao YY. Endothelial p110gammapi3k mediates endothelial regeneration and vascular repair after inflammatory vascular injury. Circulation. 2016;133:1093–1103 [PubMed: 26839042]
75. Angelidis I, Simon LM, Fernandez IE, Strunz M, Mayr CH, Greiffo FR, Tsitsiridis G, Ansari M, Graf E, Strom TM, Nagendran M, Desai T, Eickelberg O, Mann M, Theis FJ, Schiller HB. An atlas of the aging lung mapped by single cell transcriptomics and deep tissue proteomics. Nature communications. 2019;10:963
76. Zhang XA, Lane WS, Charrin S, Rubinstein E, Liu L. Ewi2/pgrl associates with the metastasis suppressor kai1/cd82 and inhibits the migration of prostate cancer cells. Cancer research. 2003;63:2665–2674 [PubMed: 12750295]
77. Schiller HB, Fernandez IE, Burgstaller G, Schaab C, Scheltema RA, Schwarzmayr T, Strom TM, Eickelberg O, Mann M. Time- and compartment-resolved proteome profiling of the extracellular niche in lung injury and repair. Molecular systems biology. 2015;11:819 [PubMed: 26174933]
78. Cox J, Hein MY, Luber CA, Paron I, Nagaraj N, Mann M. Accurate proteome-wide label-free quantification by delayed normalization and maximal peptide ratio extraction, termed maxlfq. Molecular & cellular proteomics : MCP. 2014;13:2513–2526 [PubMed: 24942700]
79. Tyanova S, Temu T, Sinitcyn P, Carlson A, Hein MY, Geiger T, Mann M, Cox J. The perseus computational platform for comprehensive analysis of (prote)omics data. Nature methods. 2016;13:731–740 [PubMed: 27348712]
80. Coumans FAW, Brisson AR, Buzas EI, Dignat-George F, Drees EEE, El-Andaloussi S, Emanueli C, Gasecka A, Hendrix A, Hill AF, Lacroix R, Lee Y, van Leeuwen TG, Mackman N, Mager I, Nolan JP, van der Pol E, Pegtel DM, Sahoo S, Siljander PRM, Sturk G, de Wever O, Nieuwland R. Methodological guidelines to study extracellular vesicles. Circulation research. 2017;120:1632–1648 [PubMed: 28495994]
81. Liu J, Lu W, Reigada D, Nguyen J, Laties AM, Mitchell CH. Restoration of lysosomal ph in rpe cells from cultured human and abca4(−/−) mice: Pharmacologic approaches and functional recovery. Investigative ophthalmology & visual science. 2008;49:772–780 [PubMed: 18235027]
82. Jumper J, Evans R, Pritzel A, Green T, Figurnov M, Ronneberger O, Tunyasuvunakool K, Bates R, Zidek A, Potapenko A, Bridgland A, Meyer C, Kohl SAA, Ballard AJ, Cowie A, Romera-Paredes B, Nikolov S, Jain R, Adler J, Back T, Petersen S, Reiman D, Clancy E, Zielinski M, Steinegger M, Pacholska M, Berghammer T, Bodenstein S, Silver D, Vinyals O, Senior AW, Kavukcuoglu K, Kohli P, Hassabis D. Highly accurate protein structure prediction with alphafold. Nature. 2021;596:583–589 [PubMed: 34265844]
83. Sastry GM, Adzhigirey M, Day T, Annabhimoju R, Sherman W. Protein and ligand preparation: Parameters, protocols, and influence on virtual screening enrichments. Journal of computer-aided molecular design. 2013;27:221–234 [PubMed: 23579614]
84. Phillips JC, Hardy DJ, Maia JDC, Stone JE, Ribeiro JV, Bernardi RC, Buch R, Fiorin G, Henin J, Jiang W, McGreevy R, Melo MCR, Radak BK, Skeel RD, Singharoy A, Wang Y, Roux B, Aksimentiev A, Luthey-Schulten Z, Kale LV, Schulten K, Chipot C, Tajkhorshid E. Scalable molecular dynamics on cpu and gpu architectures with namd. J Chem Phys. 2020;153:044130 [PubMed: 32752662]

85. Lopez CA, Zhang X, Aydin F, Shrestha R, Van QN, Stanley CB, Carpenter TS, Nguyen K, Patel LA, Chen D, Burns V, Hengartner NW, Reddy TJE, Bhatia H, Di Natale F, Tran TH, Chan AH, Simanshu DK, Nissley DV, Streitz FH, Stephen AG, Turbyville TJ, Lightstone FC, Gnanakaran S, Ingolfsson HI, Neale C. Asynchronous reciprocal coupling of martini 2.2 coarse-grained and charmm36 all-atom simulations in an automated multiscale framework. Journal of chemical theory and computation. 2022;18:5025–5045 [PubMed: 35866871]

86. Li Y, Liu J, Gumbart JC. Preparing membrane proteins for simulation using charmm-gui. Methods Mol Biol. 2021;2302:237–251 [PubMed: 33877631]

87. Pettersen EF, Goddard TD, Huang CC, Meng EC, Couch GS, Croll TI, Morris JH, Ferrin TE. Ucsf chimerax: Structure visualization for researchers, educators, and developers. Protein science : a publication of the Protein Society. 2021;30:70–82 [PubMed: 32881101]

Novelty and Significance

What Is Known?

- Tetraspanin CD151 is localized in the plasma membrane and in the endolysosome and physically associates with integrin.
- CD151 supports cell adhesion and migration and regulates cardiovascular functions including pathological angiogenesis, vascular stability, and thrombosis.

What New Information Does This Article Contribute?

- The CD151-IFITM3 complex restrains exosomal discharge of proteins, and confines vascular inflammation.
- CD151 facilitates VCP/p97-mediated turnover of IFITM3 and V-ATPase, maintaining the integrity of endolysosomes and exosomes.
- This modulation of protein control in endolysosomes and the balancing lysosomal degradation versus exosomal protein discharge may be possible therapeutic strategies for regulating vascular inflammation.

Endolysosomes are increasingly recognized as metabolism-regulatory hubs, but their contributions to inflammation are still elusive. Despite CD151 abundance in endolysosomes, their endolysosomal function and role in vascular inflammation are unknown. We found that endothelial CD151 is down-regulated in inflammation and restrains pulmonary and cardiac inflammation, and severe sepsis in animal models. CD151 regulates endolysosome functions by maintaining endolysosomal protein quality. CD151 docks valosin-containing protein (VCP)/p97 onto endolysosomes to facilitate deubiquitination. Also, CD151 bridges VCP/p97 interactions with IFITM3 and V-ATPase and promotes V-ATPase assembly allowing for endolysosome mediated degradation. We also found IFITM3 is up-regulated in inflammation and supports discharge of pro-inflammatory molecules through exosomes. Thus, the IFITM3/V-ATPase-tetraspanin-VCP/p97 complex influences endolysosome function and modulates inflammation.

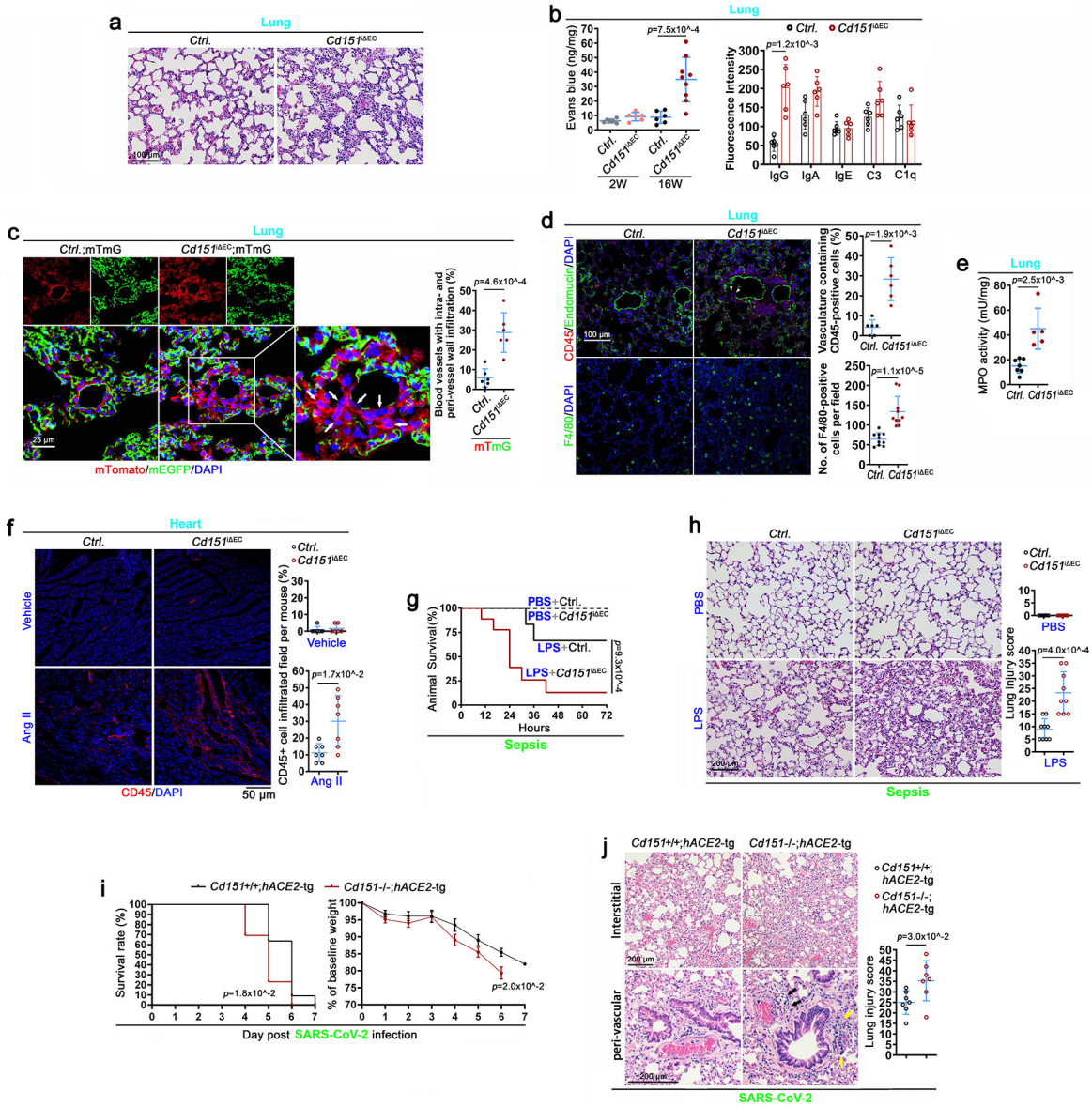

Figure 1. Endothelium-specific ablation of *Cd151* leads to pulmonary inflammation and escalates vascular inflammatory responses.

a: H&E staining of lung sections from control (*Ctrl.*) and *Cd151*$^{i\Delta EC}$ mice with age of 22 weeks. All mice were treated with tamoxifen. **b: Left:** Miles assay of *Ctrl.* and *Cd151*$^{i\Delta EC}$ mouse lungs was performed at 2 and 16 weeks after tamoxifen injection. Extravasated Evans blue was quantified and is presented as mean±*SD* (*n*=6 mice for *Ctrl.* group and *n*=9 mice for *Cd151*$^{i\Delta EC}$ group). **Right:** Lung sections from *Ctrl.* and *Cd151*$^{i\Delta EC}$ mice were stained for IgG, IgA, and IgE and C3 and C1q with immunofluorescence. Levels of these proteins are projected by their fluorescence intensities (mean±SD, *n*=6 mice for each group). Representative images are shown in Figure S3b-c. **c**: Fluorescence microscopic images of the lung sections from *Ctrl.;mTmG*$^{+}$ and *Cd151*$^{i\Delta EC}$*;mTmG*$^{+}$ mice. Percentages of blood vessels with intra- and peri-vessel wall infiltration were presented as mean±*SD* (*n*=6 mice per group). **d**: Immunofluorescence of lung sections from *Ctrl.*

and *Cd151*$^{i\Delta EC}$ mice. Percentages of blood vessels with the CD45^{+} cell infiltration are presented as mean±*SD* (*n*=6 mice per group). Numbers of F4/80^{+} cell are presented as mean±*SD* (*n*=10 mice for each group). **e**: MPO activities of the lung tissues from *Ctrl.* and *Cd151*$^{i\Delta EC}$ mice (mean±*SD*, *n*=7 mice for *Ctrl.* group and *n*=5 mice for *Cd151*$^{i\Delta EC}$ group). **f**: *Ctrl.* and *Cd151*$^{i\Delta EC}$ mice were infused with angiotensin II (Ang II, diluted in saline, 1mg/kg/day) or vehicle (saline) for 28 days. Mouse heart sections were stained with CD45 antibody (Red) and DAPI (Blue). Leukocyte infiltration is presented as the percentage of the fields containing CD45^{+} cell per mouse (mean±*SD*, *n*=6 mice for *Ctrl.*+Vehicle or *Cd151*$^{i\Delta EC}$+Vehicle group, *n*=7 mice for *Ctrl.*+Ang II or *Cd151*$^{i\Delta EC}$+Ang II group). **g**: Kaplan-Meier curves of *Ctrl.* and *Cd151*$^{i\Delta EC}$ mice in LPS-caused sepsis. The mice were challenged with LPS (18 mg/kg, i.p.) or PBS (groups PBS+*Ctrl.*: *n*=10 mice, PBS+*Cd151*$^{i\Delta EC}$: *n*=10 mice, LPS+*Ctrl.*: *n*=9 mice, and LPS+*Cd151*$^{i\Delta EC}$: *n*=8 mice), and their survival rates were evaluated by Kaplan-Meier curves and compared by Log-rank (Mantel-Cox) test. **h**: *Ctrl.* and *Cd151*$^{i\Delta EC}$ mice were treated with LPS (12 mg/kg, i.p.) or PBS for 12 hours, H&E staining of the lung sections was performed, and pathological changes were graded as lung injury score (mean±*SD*, groups PBS+*Ctrl.*: *n*=6 mice, PBS+*Cd151*$^{i\Delta EC}$: *n*=6 mice, LPS+*Ctrl.*: *n*=9 mice, and LPS+*Cd151*$^{i\Delta EC}$: *n*=9 mice). **i:** *Cd151* removal exacerbates Covid19 progression. **Left:** the mice were challenged with SARS-CoV-2. Mouse survival rates were determined as described above. **Right:** changes in body weight were monitored and are presented as percentage of initial weight (*Cd151*$^{+/+}$;*hACE2-tg* group: n=11 mice; *Cd151*$^{-/-}$;*hACE2*-tg group: n=13 mice). **j:** *Cd151* removal worsens lung inflammation of Covid19. H&E staining of lung sections from the mice that were infected with SARS-CoV-2 and ended at the 5th day after the infection was graded for lung injury score (mean±*SD*, *Cd151*$^{+/+}$;*hACE2-tg* group: n=7 mice; *Cd151*$^{-/-}$;*hACE2*-tg group: n=7 mice). Arrows: infiltrated inflammatory cells (Yellow: peri-bronchi area; Black: peri-vessel area). Methods of statistical analysis are listed in Supplemental Table S1.

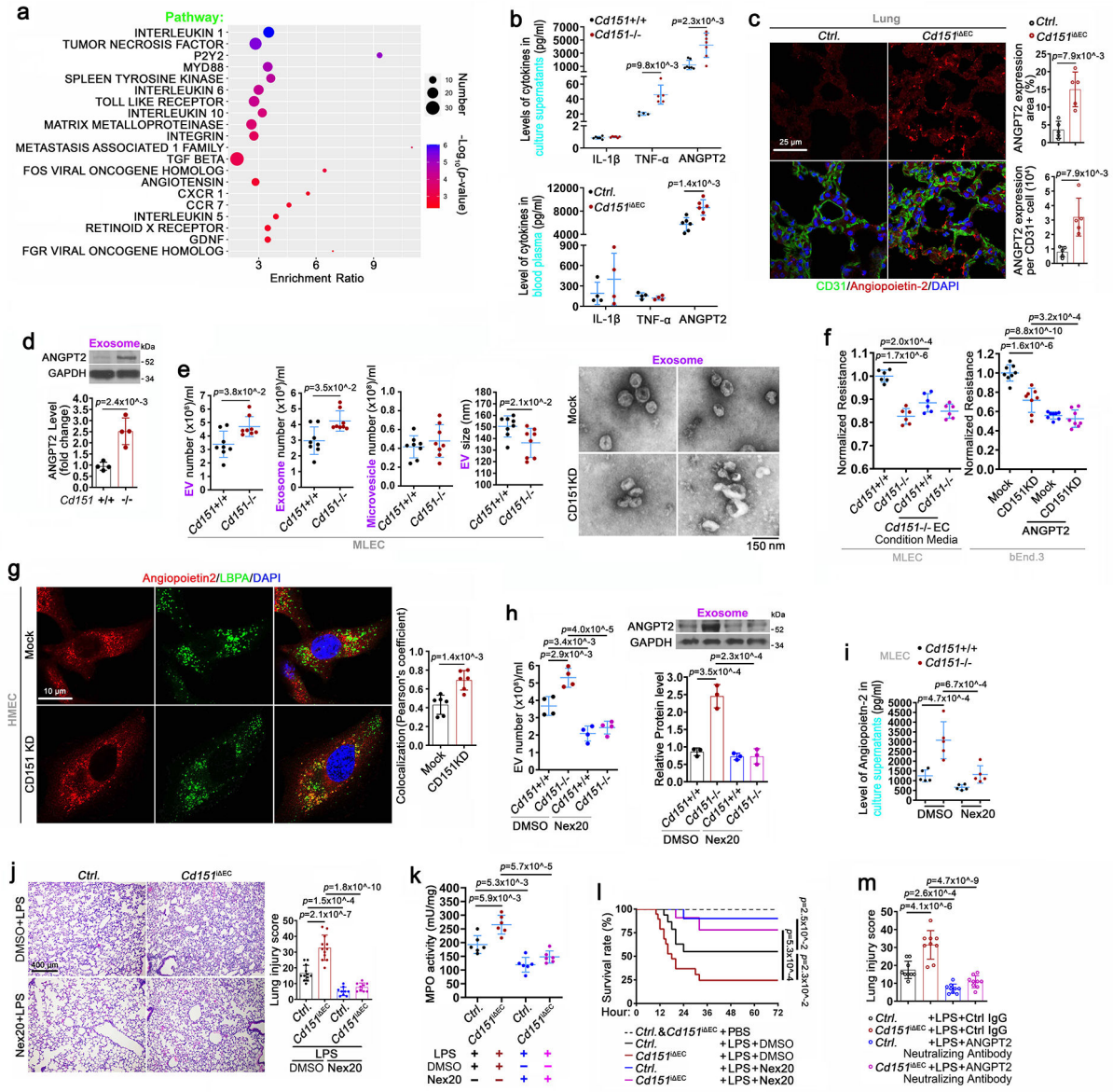

Figure 2. Endothelial removal of CD151 promotes exosomal release of Angiopoietin-2 (ANGPT2).

a: Top 20 signaling pathways associated with endothelial *Cd151* ablation, based on RNA-seq of *Cd151*$^{-/-}$ versus *Cd151*$^{+/+}$ MLECs, are listed according to their *p*-values. The bubble chart of gene set enrichment ratio was performed with Rstudio software and the Genomatix Pathways System. **b:** Levels of IL-1β, TNF-α, and ANGPT2 in the culture supernatants of primary MLECs isolated from 8~12-week-old mice (**upper**) and blood plasma of *Ctrl.* and *Cd151*$^{i\Delta EC}$ mice (**lower**). Results are presented as mean±*SD* (*n*=7 individual experiments for *Cd151*$^{+/+}$ or *Cd151*$^{-/-}$ group; *n*=6 mice for *Ctrl.* or *Cd151*$^{i\Delta EC}$ group). Panels of cytokine secretomes are shown in Figure S5a-b. **c:** Tissue distribution of ANGPT2. Mouse lung sections were stained for CD31 (green), ANGPT2 (red), and nucleus (blue) and imaged. ANGPT2 expression in lungs were quantified as fluorescence area per field (%) and fluorescence intensity per CD31^{+} cell (mean±*SD*, *n*=5 mice for each group).

d: Exosomal ANGPT2 and cytoplasmic GAPDH proteins from MLECs were examined with Western blot and quantified as band densities. CD151 band densities were normalized by the band densities of loading control GAPDH and presented as the levels relative to its normalized density in *Cd151*$^{+/+}$ group (Mean±*SD*, *n*=4 individual experiments). **e:** EVs from *Cd151*$^{-/-}$ and *Cd151*$^{+/+}$ MLECs were detected by Nanosight. Concentrations of EVs (20-1,000nm), exosome (20-200nm), and microparticles (200-1,000nm) and their sizes are presented as mean±*SD* (*n*=8 individual experiments). TEM images of the isolated exosomes from bEnd.3-Mock and -CD151KD cells. **f:** TEER of the MLEC monolayers treated with or without the condition media (C.M.) of *Cd151*$^{-/-}$ MLECs was measured (mean±*SD*, *n*=6 individual experiments). TEER of bEnd.3-Mock and -CD151KD monolayers treated with or without angiopoietin-2 (ANGPT2, 100 ng/ml) was measured (mean±*SD*, *n*=8 individual experiments). **g:** The HMECs were stained for ANGPT2 and LBPA, and their colocalization was then examined in immunofluorescence with confocal microscopy and quantified as Pearson's coefficients (mean±*SD*, *n*=6 individual experiments). **h:** Effects of Nex20 on EV and exosomal ANGPT2. **Left:** EVs from the *Cd151*$^{-/-}$ and *Cd151*$^{+/+}$ MLECs treated with Nex20 (dissolved in DMSO, 5 μM) or DMSO for 4h were detected by Nanosight. Total EVs concentration are presented as mean±*SD* (*n*=4 individual experiments). **Right**: ANGPT2 proteins in the exosomes were examined by Western blot and quantified as band densities as described above (mean±*SD*, *n*=3 individual experiments). **i:** Primary MLECs were treated with Nex20 (5 μM) or DMSO for 4h. Levels of ANGPT2 in the culture supernatants of the MLECs were measured, and the results are presented as mean±*SD* (*n*=5 individual experiments). **j**: *Ctrl.* and *Cd151*$^{i\Delta EC}$ mice were treated with LPS (12 mg/kg) and Nex20 (15 mg/kg) or vehicle (DMSO). Nex20 was injected into mice intraperitoneally 3 hours prior to LPS administration. Lung injury scores based on H&E staining were measured and are presented as mean±*SD* (groups LPS+Vehicle+*Ctrl.*: *n*=12 mice, LPS+Vehicle+*Cd151*$^{i\Delta EC}$: *n*=12 mice, LPS+Nex20+*Ctrl.*: *n*=9 mice, and LPS+Nex20+*Cd151*$^{i\Delta EC}$: *n*=9 mice). **k:** *Ctrl.* and *Cd151*$^{i\Delta EC}$ mice were treated with LPS (12 mg/kg) and Nex20 (15 mg/kg) or vehicle. Nex20 was injected into mice intraperitoneally 3 hours prior to LPS administration. MPO activities of lung tissues were measured and is presented as mean±*SD* (*n*=6 mice/group). **l:** *Ctrl.* and *Cd151*$^{i\Delta EC}$ mice were treated with LPS (18 mg/kg) and Nex20 (15 mg/kg) or vehicle (DMSO). Nex20 or vehicle was injected into mice intraperitoneally 3 hours prior to LPS administration. The animal survivals were monitored (Vehicle+*Ctrl.* group: *n*=15 mice; Vehicle+*Cd151*$^{i\Delta EC}$: *n*=15 mice; Vehicle+LPS+*Ctrl.*: *n*=21 mice; Vehicle+LPS+*Cd151*$^{i\Delta EC}$: *n*=20 mice; Nex20+LPS+*Ctrl.*: *n*=21 mice; and Nex20+LPS+*Cd151*$^{i\Delta EC}$: *n*=20 mice), and their survival rates were determined as described above. **m:** *Ctrl.* and *Cd151*$^{i\Delta EC}$ mice were treated with the neutralizing antibody against murine ANGPT2 (dissolved in PBS, 4 mg/kg, i.p.) or control IgG. After 24 h, LPS (12 mg/kg, i.p.) was administered. Lungs were harvested at 12 h after the administration, sectioned, and processed for H&E staining. Lung injury scores were assessed and are presented as mean±*SD* (*n*=9 mice/group). Representative images are shown in Figure S5e. Methods of statistical analysis are listed in Supplemental Table S1.

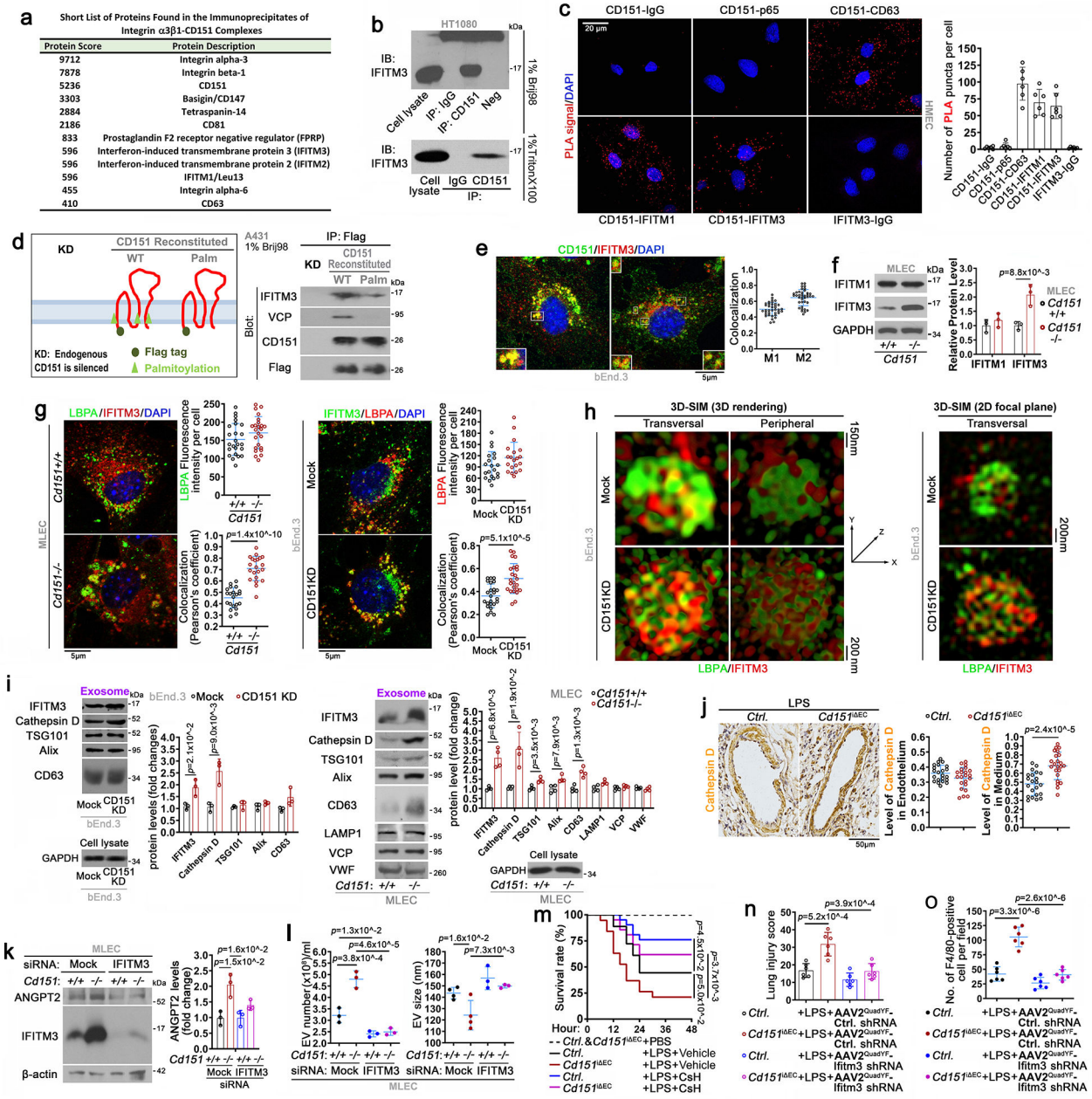

Figure 3. Physical association of CD151 with IFITM3 and its functional effects.

a: Immunoprecipitate of integrin α3-CD151 complex was acquired by human integrin α3 mAb IVA5 and analyzed with NanoLC ion trap MS/MS proteomics technology. Proteins precipitated with the complexes and with score>400 were listed. **b:** Co-immunoprecipitation (co-IP) with human CD151 mAb 11G5α and mouse IgG and immunoblot with IFITM3 Ab were performed in HT1080 under 1% Brij-98 and 1% Triton X-100 lysis conditions. Neg: 11G5α was incubated with lysis buffer and precipitated by the beads. **c:** Interactions between indicated proteins were examined with PLA in HMECs. PLA signals, in red fluorescence, were quantified and are presented as mean±*SD* (*n*=6 individual experiments). **d:** Importance of CD151 palmitoylation for the IFITM3-CD151-VCP complex formation.

Left: Schematic presentation of CD151 reconstitution in CD151-silenced A431 cells, including CD151 wildtype (WT) and CD151 palmitoylation-deficient mutant (Palm). **Right:** A431 cells were lyzed with 1% Brij-98 lysis buffer, and the lysates were immunoprecipitated with Flag antibody and immunoblotted for IFITM3, VCP, CD151, and Flag tag. **e:** Distributions of the indicated proteins in bEnd.3 ECs were examined in immunofluorescence with confocal microscopy, and their colocalizations were quantified as Manders' coefficients (n=20 cells). Insets present magnified portions of the images. **f:** Levels of IFITM1 and IFITM3 proteins in *Cd151*$^{+/+}$ and *Cd151*$^{-/-}$ MLECs were detected by Western blot and are presented as band densities, which were normalized by the band densities of loading control GAPDH and presented as the levels relative to the normalized density of the same protein in *Cd151*$^{+/+}$ group (mean±*SD*, n=3 individual experiments). **g:** IFITM3 and LBPA in *Cd151*$^{+/+}$ and *Cd151*$^{-/-}$ MLECs, Mock and CD151KD of bEnd.3 cells were examined in immunofluorescence with confocal microscopy. LBPA and IFITM3-LBPA colocalization were quantified and are presented as fluorescence intensity per cells and Pearson's coefficient (mean±*SD*, n=20 cells/group), respectively. Images of separated channels are shown in Figure S6f. **h:** IFITM3 and LBPA in bEnd.3-Mock and -CD151KD cells were examined by immunofluorescence with Structured Illumination Microscopy (SIM). **Left:** shown are the transversal and peripheral views of MVBs from 3D reconstruction of the staining (The side view is shown in Figure S6g**); Right:** shown are single focal plane. **i:** Indicated proteins in the exosomes purified from culture supernatants of bEnd.3 cells (**left**) and MLECs (**right**) were examined with Western blot and are quantified by band densities as described above (mean±*SD*, n=3 individual experiments for bEnd.3 cells and n=4 for MLECs). **j:** Lung sections from *Ctrl.* and *Cd151*$^{i\Delta EC}$ mice treated with LPS (12 mg/kg, i.p., 12 hours) were stained in immunohistochemistry with Cathepsin D Ab. Cathepsin D protein levels in endothelium and medium of blood vessels were quantified and are presented as OD value (mean±*SD,* n=22 images/group, 3~5 images per optical plane and 4~5 optical planes per mouse lung were analyzed for each group which contains 5 mice, and each data dot indicates the average signal density of each optical plane). **k:** MLECs were transfected with control or IFITM3 siRNA. IFITM3 and ANGPT2 protein were examined with Western blot and quantified as band densities as described above (mean±*SD*, n=3 individual experiments). **l:** MLECs were transfected with control or IFITM3 siRNA. At 48 hours after the transfection, EVs in the culture supernatants were analyzed by Nanosight and quantified as number and size (mean±*SD*, n=3 individual experiments). **m:** *Ctrl.* and *Cd151*$^{i\Delta EC}$ mice were treated with LPS (18mg/kg) and CsH (2 mg/kg) or vehicle, which was injected i.p. at 3 hours prior to LPS administration. The mice (groups Vehicle+*Ctrl.*: n=14 mice; Vehicle+*Cd151*$^{i\Delta EC}$: n=15; Vehicle+LPS+*Ctrl.*: n=18; Vehicle+LPS+*Cd151*$^{i\Delta EC}$: n=19; CsH+LPS+*Ctrl.*: n=21; and CsH+LPS+*Cd151*$^{i\Delta EC}$: n=21) were monitored for survival, and their survival rates were assessed as described in Methods. **n**: *Ctrl.* and *Cd151*$^{i\Delta EC}$ mice received AAV2^{QuadYF}-scramble shRNA or AAV2^{QuadYF}-Ifitm3 shRNA (diluted in 200 μl PBS) via tail vein injection. After two weeks, acute lung injury was induced by LPS (12 mg/kg) as described above. Mouse lungs were harvested at 12 h after LPS administration, sectioned, and processed for H&E staining. Lung injury scores were assessed and are presented as mean±*SD* (n=6 mice/group). Representative images are shown in Figure S7f. **o**: Lung sections from the experiments described in panel **n** were stained for F4/80 in immunofluorescence. Number of F4/80^{+} cell is presented as mean±*SD*

(n=6 mice/group). Representative images are shown in Figure S7g. Methods of statistical analysis are listed in Supplemental Table S1.

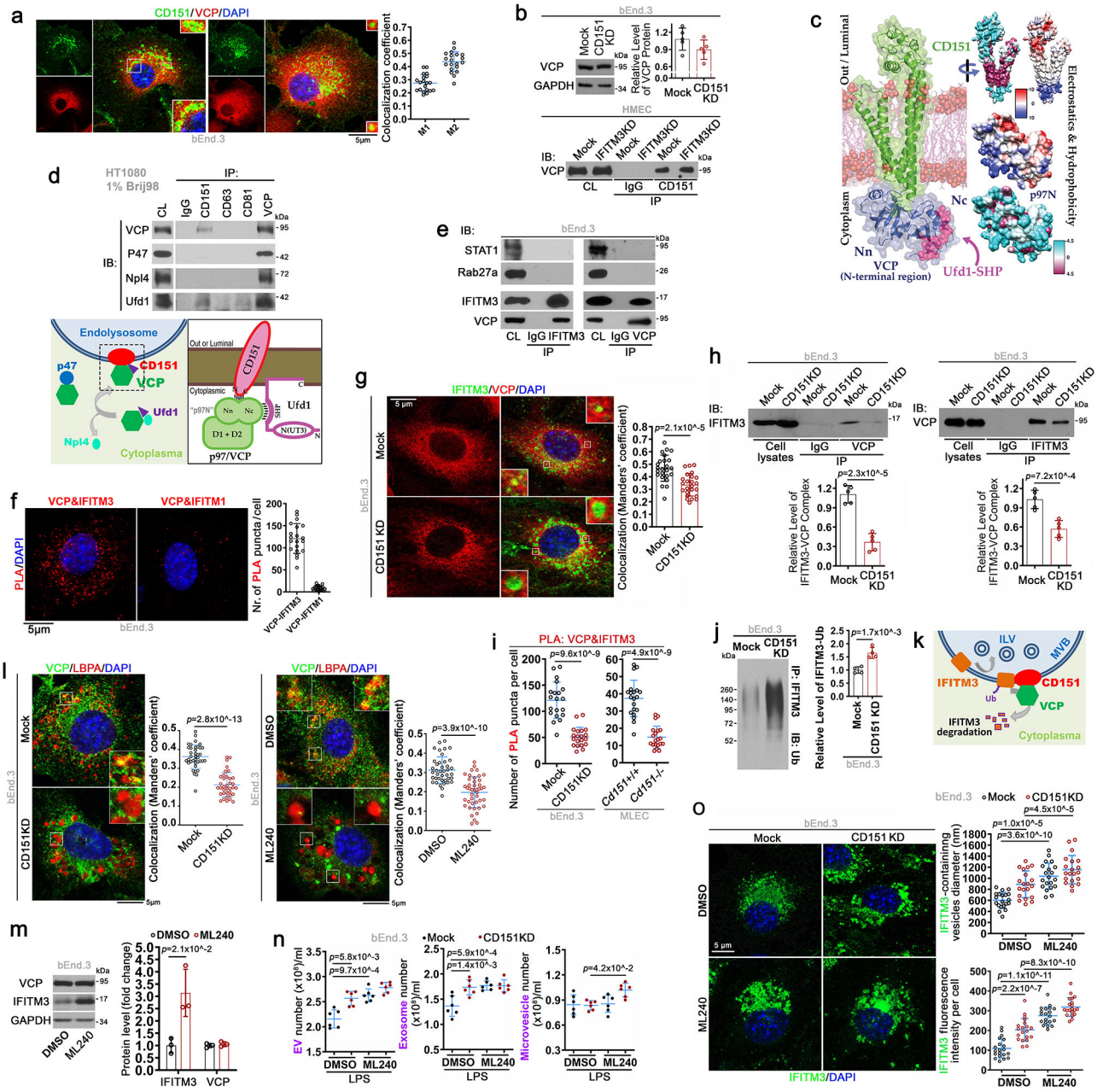

Figure 4. Importance of IFITM3 for CD151 activities and of CD151 for VCP-IFITM3 association

a: Distributions of CD151 and VCP in bEnd.3 ECs were examined in immunofluorescence with confocal microscopy, and their colocalizations were quantified as Manders' coefficients (mean±*SD*, *n*=20 cells). **b: top**: VCP proteins in bEnd.3 transfectants were examined in Western blot and quantified as band densities, which were normalized by the band densities of loading control GAPDH and presented as the levels relative to its normalized density in Mock group (mean±*SD*, *n*=5 individual experiments). **bottom**: The 1%Brij98 lysates of HMEC-Mock and -IFITM3KD cells were immunoprecipitated with human CD151 mAb (11G5a), followed by immunoblot for VCP. CL: cell lysates. **c:** Molecular dynamics and modeling of CD151-p97 N-terminal domain (p97N) interaction. **Left**: CD151 (green,

generated using AlphaFold) embedded in a POPC membrane interacting with the N-terminal p97N binding module (blue, PDB 5B6C) following 500 ns of atomistic molecular dynamics. The SHP-binding domain of Ufd1 is shown as spheres (magenta). Resulting model shows that CD151 cytoplasmic termini and loop form a stable binding with the Nn-Nc binding cleft of p97N. **Right**: This binding is stabilized by both electrostatic and hydrophobic interactions: electrostatic (blue and red) and hydrophobicity (magenta and cyan) surface models shown for p97N and CD151. CD151 is rotated 180° while p97N is oriented to match MD docking results. **d:** CD151-VCP association independent of p47 and Npl4. **Upper:** HT1080 cells were lyzed with 1% Brij-98 lysis buffer, and the lysates were immunoprecipitated with mouse IgG, CD151 mAb (11G5α), CD63 mAb, CD81 mAb, and VCP mAb, followed by immunoblots for VCP, P47, Npl4, and Ufd1. **Lower:** Schematic representation of the CD151-VCP-Ufd1 interaction. This model shows a direct binding between CD151 (red) and p97 N-terminal domain (green), which anchors p97 near the membrane. Ufd1 (purple) binds directly to p97 through the SHC motif forming a ternary complex. **e:** The 1%Brij-98 lysates of bEnd.3 ECs were immunoprecipitated with IgG, IFITM3 Ab, and VCP Ab, followed by immunoblot for indicated proteins. CL: cell lysates. **f:** Interactions between indicated proteins were examined with PLA in bEnd.3 ECs. PLA signals, in red fluorescence, were quantified (mean±*SD*, n=20 cells). Scale bar: 5 μm. **g:** Colocalization of IFITM3 with VCP in bEnd.3 ECs was examined in immunofluorescence with confocal microscopy and quantified as Manders' coefficient (mean±*SD*, n=20 cells per group). Insets present magnified portions of the images. **h:** Association of IFITM3 and VCP in bEnd.3 ECs was examined by their co-immunoprecipitation under 1%Brij-98 lysis condition and quantified as band densities as described above (mean±*SD*, n=5 individual experiments). **i:** Interaction between IFITM3 and VCP in bEnd.3 ECs and MLECs was examined with PLA. PLA signals, in red fluorescence, were quantified (mean±*SD*, n=20 cells). Representative images are shown in Figure S8f**. j:** bEnd.3 ECs were treated with MG132 (10 μM) for 2 h prior to lysis with 1% Triton X-100 buffer. The lysates were immunoprecipitated with IFITM3 Ab, and the precipitates were immunoblotted with ubiquitin Ab and quantified as band densities as described above (mean±*SD*, n=4 individual experiments). **k:** Schematic diagram for IFITM3-CD151-VCP complex. **l:** Colocalizations of LBPA with VCP, in bEnd.3-Mock and -CD151KD transfectants (**Left**) and in bEnd.3 ECs treated with control (DMSO) and VCP inhibitor ML240 (1 mM, diluted in DMSO) for 12 h (**Right**), were examined in immunofluorescence with confocal microscopy and quantified as Manders' coefficients (mean±*SD*, n=40 cells per group). **m:** The cells were treated with ML240 (1 μM) at 37°C for 6 h, followed by cell lysis; and the indicated proteins were examined with Western blot and quantified by band densities as described above (mean±*SD*, n=3 individual experiments). **n:** EVs from the bEnd.3 ECs treated with LPS (1 μg/ml) and ML240 (1 μM) or control (DMSO) for 4 h were analyzed by Nanosight and quantified as number/ml (mean±*SD*, n=6 individual experiments). **o:** Immunofluorescence of IFITM3 in the bEnd.3 ECs treated with ML240 (1 μM) or control (DMSO) for 12 h was analyzed with confocal microscopy, and size of IFITM3-positive vesicles and IFITM3 fluorescence intensity were quantified (mean±*SD*, n=20 cells per group). Methods of statistical analysis are listed in Supplemental Table S1.

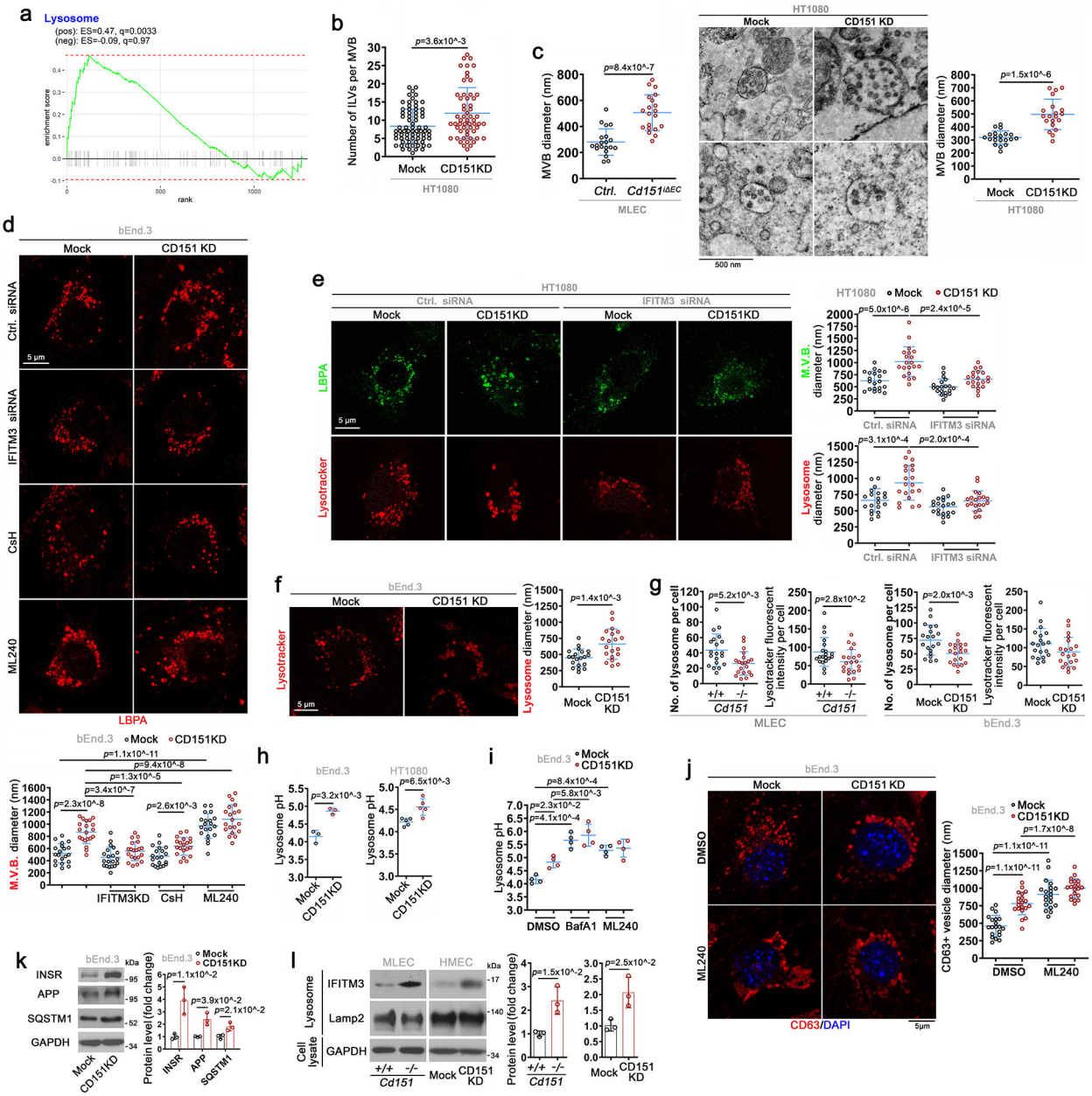

Figure 5. IFITM3-CD151-VCP complexes are required for the structural and functional integrity of MVBs/lysosomes.

a: Gene set enrichment analysis for proteins in the lysosome pathway, ranked by log2-transformed fold change. **b**: Numbers of intraluminal vesicle (ILV) in MVBs of HT1080 transfectants were quantified based on TEM analysis (mean±*SD*, *n*=60 cells per group). **c**: TEM analysis on MVBs in MLECs and HT1080 cells. MVB diameter was measured manually and is presented as mean±*SD* (*n*=20 cells per group). **d**: bEnd.3 ECs were treated with either IFITM3 siRNA (for 48 h), CsH (2.5 μM for 12 h), or ML240 (1 μM for 12 h), stained for LBPA in immunofluorescence, and examined with confocal microscopy. Size of vesicle is presented as average diameter of puncta within a cell (mean±*SD*, *n*=20 cells per group). **e**: HT1080-Mock and -CD151KD cells were transfected with control or IFITM3

siRNA and then stained with LBPA Ab or lysotracker and photographed with fluorescence confocal microscopy. Size of vesicle is presented as average diameter of puncta within a cell (mean±*SD*, n=20 cells per group). **f**: Mock and CD151KD transfectants of bEnd.3 ECs were incubated with lysotracker (1 μM) at 37 °C for 30 min and imaged with confocal microscopy. Lysosomes were quantified as the average diameter of puncta within a cell (mean±*SD*, n=20 cells per group). **g**: Lysosomes, revealed by lysotracker staining, in bEnd.3 and MLECs were quantified as numbers and fluorescence intensity per cell (mean±*SD*, n=20 cells per group). **h**: Lysosome pH was measured by incubation of bEnd.3 and HT1080 cells with LysoSensor™ Yellow/Blue DND-160 (3 μM) at 37°C for 10 min. By standard curve with a pH range of 3.5-6.0, the fluorescence intensity was converted to pH (mean±*SD*, n=3 individual experiments for bEnd.3 cells and n=5 for HT080 cells, **: p<0.01). **i**: Lysosome pH of the bEnd.3 cells treated with bafilomycin-A1 (BafA1) (200 nM) or ML240 (1 μM) for 1h was measured as described above and is presented as mean±*SD* (n=4 individual experiments). **j**: Mock and CD151KD transfects of bEnd.3 ECs were treated with ML240 (1 μM) for 12 h, then stained with CD63 mAb, and photographed with fluorescence confocal microscopy. Size of CD63-positive vesicle is presented as average diameter of puncta within a cell (mean±*SD*, n=20 cells per group). **k**: Indicated proteins in the lysates of bEnd.3-Mock and -CD151KD cells were examined with Western blot and quantified as band densities, which were normalized by the band densities of loading control GAPDH and presented as the levels relative to the normalized density of the same protein in Mock group (mean±*SD*, n=3 individual experiments). **l**: Indicated proteins of the purified lysosomes from MLECs and HMECs were examined with Western blot and quantified by band densities as described above (mean±*SD*, n=3 individual experiments). Methods of statistical analysis are listed in Supplemental Table S1.

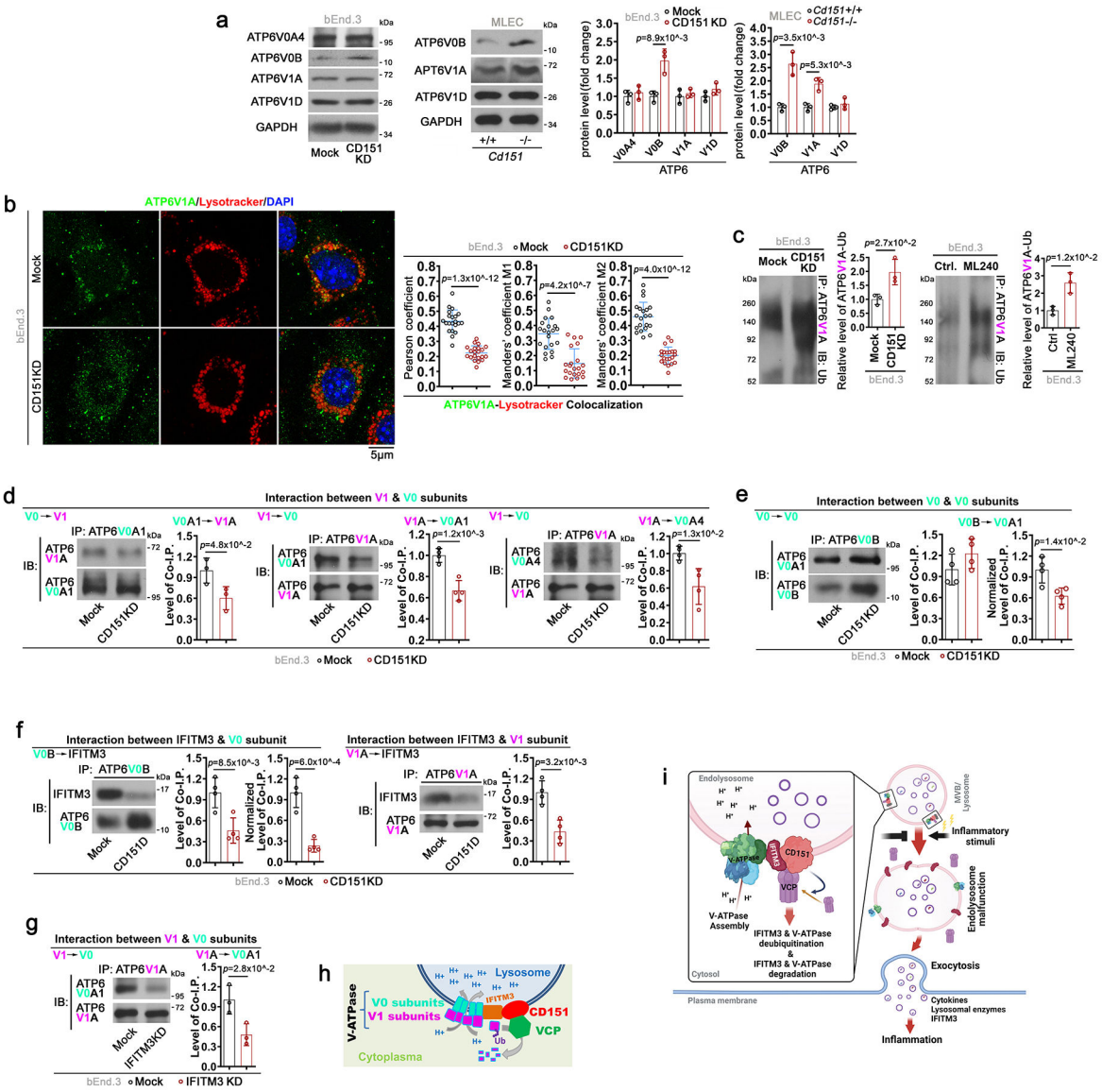

Figure 6. IFITM3-CD151-VCP complexes are required for proper assemble of V-ATPase of lysosomes

a: Protein levels of V-ATPase subunits in bEnd.3 ECs and MLECs were examined with Western blot and quantified by band densities, which were normalized by the band densities of loading control GAPDH and presented as the levels relative to the normalized density of the same protein in Mock or *Cd151*$^{+/+}$ group (mean±*SD*, *n*=3 individual experiments). **b**: Colocalization of ATP6V1A with lysotracker in bEnd.3-Mock and -CD151KD cells was examined in immunofluorescence with confocal microscopy and quantified as Pearson's and Manders' coefficients (mean±*SD*, *n*=20 cells per group). **c**: After being treated with or without MG132 (10 μM) at 37°C for 2 h, bEnd.3 ECs were lyzed with 1% Triton X-100 buffer. The lysates were immunoprecipitated with ATP6V1A Ab, and the precipitates were immunoblotted with ubiquitin Ab and quantified by band densities as described above (mean±*SD*, *n*=3 individual experiments). **d**: Physical interactions between cytoplasmic and transmembrane subunits of V-ATPase in bEnd.3 transfectants were examined by co-

immunoprecipitation after cell lysis with 1% Triton X-100 buffer and quantified by band densities as described above (mean±*SD*, *n*=4 individual experiments). **e**: Physical interaction between transmembrane subunits of V-ATPase in bEnd.3 transfectants was examined by co-immunoprecipitation after cell lysis with 1% Triton X-100 buffer and quantified by band densities as described above (mean±*SD*, *n*=4 individual experiments). **f**: Physical interactions between IFITM3 and V-ATPase subunits in bEnd.3 transfectants were examined by co-immunoprecipitation after cell lysis with 1% Triton X-100 buffer and quantified by band densities as described above (mean±*SD*, *n*=4 individual experiments). **g**: Physical interactions between V-ATPase subunits in bEnd.3-Mock and -IFITM3KD transfectants were examined by co-immunoprecipitation after cell lysis with 1% Triton X-100 buffer and quantified by band densities as described above (mean±*SD*, *n*=3 individual experiments). **h**: Schematic presentation of functional crosstalk between CD151 and V-ATPase on endolysosome. **i**: Graphic abstract (created with BioRender.com). Methods of statistical analysis are listed in Supplemental Table S1.